

Two-dimensional modelling of subduction zone anisotropy with application to southwestern Japan

Maureen D. Long,¹ ★ Bradford H. Hager,¹ Maarten V. de Hoop² and Rob D. van der Hilst¹

¹*Department of Earth, Atmospheric, and Planetary Sciences, Massachusetts Institute of Technology, 77 Massachusetts Ave., Cambridge, MA 02139, USA.
E-mail: mlong@alum.mit.edu*

²*Center for Computational and Applied Mathematics, Purdue University, 150 N. University St., W. Lafayette, IN 47907, USA*

Accepted 2007 April 3. Received 2007 March 1; in original form 2006 August 23

SUMMARY

We present a series of 2-D numerical models of viscous flow in the mantle wedge induced by a subducting lithospheric plate. We use a kinematically defined slab geometry approximating the subduction of the Philippine Sea plate beneath Eurasia. Through finite element modelling we explore the effects of different rheological and thermal constraints (e.g. a low-viscosity region in the wedge corner, power law versus Newtonian rheology, the inclusion of thermal buoyancy forces and a temperature-dependent viscosity law) on the velocity and finite strain field in the mantle wedge. From the numerical flow models we construct models of anisotropy in the wedge by calculating the evolution of the finite strain ellipse and combining its geometry with appropriate elastic constants for effective transversely isotropic mantle material. We then predict shear wave splitting for stations located above the model domain using expressions derived from anisotropic perturbation theory, and compare the predictions to ~500 previously published shear wave splitting measurements from seventeen stations of the broad-band F-net array located in southwestern Japan. Although the use of different model parameters can have a substantial effect on the character of the finite strain field, the effect on the average predicted splitting parameters is small. However, the variations with backazimuth and ray parameter of individual splitting intensity measurements at a given station for different models are often different, and rigorous analysis of details in the splitting patterns allows us to discriminate among different rheological models for flow in the mantle wedge. The splitting observed in southwestern Japan agrees well with the predictions of trench-perpendicular flow in the mantle wedge along with B-type olivine fabric dominating in a region from the wedge corner to about 125 km from the trench.

Key words: deformation, finite-element methods, seismic anisotropy, shear wave splitting, subduction zone, upper mantle.

1 INTRODUCTION

Subduction zones, regions where slabs of dense oceanic lithosphere descend into the deeper mantle, are among the most complicated tectonic environments on Earth, and even first-order aspects of their structure and dynamics are not well understood (Stern 2002). For example, the pattern of flow that is induced in the mantle wedge due to viscous coupling with the downgoing slab, flow around the slab edge, or the forces associated with slab rollback are in general not well constrained for subduction systems. One tool for probing the geometry of deformation associated with subduction is the measure-

ment of shear wave splitting, a consequence of seismic anisotropy. Anisotropy in the upper mantle can arise when mantle material, composed of individual anisotropic mineral crystals, is subjected to strain and develops a lattice preferred orientation (LPO). If the relationships among deformation, LPO, anisotropy and shear wave splitting are known or assumed, then measurements of shear wave splitting at seismic stations located above subduction zones can shed light on the style of mantle deformation associated with subduction.

Upper-mantle anisotropy related to deformation in subduction zone environments has been well-documented in a variety of regions (e.g. Ando *et al.* 1983; Fischer *et al.* 1998; Smith *et al.* 2001; Anderson *et al.* 2004; Currie *et al.* 2004; Anglin & Fouch 2005; Long & van der Hilst 2005, 2006); however, quantitative interpretation of shear wave splitting measurements in the context of a subduction zone is not straightforward. The character of splitting

★Now at: Department of Terrestrial Magnetism, Carnegie Institution of Washington, 5241 Broad Branch Road, NW, Washington, DC 20015, USA.

observations varies greatly from region to region (see Wiens & Smith 2003 for a review), and the interpretation of splitting observations is non-unique because there are many different processes that could potentially contribute to anisotropy (e.g. Park & Levin 2002). For example, both trench-parallel (e.g. Russo & Silver 1994; Gledhill & Gubbins 1996; Peyton *et al.* 2001; Anderson *et al.* 2004) and trench-perpendicular (e.g. Fischer & Yang 1994; Currie *et al.* 2004) fast directions have been observed in different regions. Several studies have noted a change in orientation of the fast splitting direction from trench-parallel close to the trench to trench-perpendicular farther from the trench (Margheriti *et al.* 1996; Smith *et al.* 2001; Nakajima & Hasegawa 2004; Long & van der Hilst 2005), although the opposite trend has also been observed (Levin *et al.* 2004). This diversity, along with the complexity of splitting patterns measured at individual stations (e.g. Helffrich *et al.* 2002; Long & van der Hilst 2005; Pozgay *et al.* 2007), is difficult to explain with a simple model for anisotropy. In contrast, the ridge-normal fast directions observed at oceanic spreading centres are relatively well understood and well explained by a simple model (e.g. Wolfe & Solomon 1998; Harmon *et al.* 2004).

A promising approach towards a rigorous interpretation of shear wave splitting measurements is to compare them with the predictions of numerical and experimental flow models and thus narrow the class of plausible models that can explain a given dataset. This approach has been taken for both global- and regional-scale problems (e.g. Becker *et al.* 2003; Behn *et al.* 2004) as well for the specific problem of subduction zone deformation (Fischer *et al.* 2000; Hall *et al.* 2000; Blackman & Kendall 2002). Much progress has been made recently on the problem of modelling subduction zone deformation (see van Keken 2003 for a review). Various numerical modelling studies have employed both kinematically (Hall *et al.* 2000; Rupke *et al.* 2004) and dynamically (Kincaid & Sacks 1997; Billen *et al.* 2003) driven slabs. Recent modelling studies have explored the effect of temperature-dependent viscosity (Eberle *et al.* 2002), a low-viscosity wedge (Billen & Gurnis 2001) and backarc spreading (Conder *et al.* 2002) on the pattern of flow in the mantle wedge. The effects of dehydration reactions and fluid release on the dynamics of the wedge have also been explored through numerical modelling studies (van Keken *et al.* 2000; Rupke *et al.* 2004; Arcay *et al.* 2005). The 3-D pattern of flow associated with phenomena such as slab rollback has been explored mainly through laboratory studies (Buttles & Olson 1998; Funiello *et al.* 2003; Kincaid & Griffiths 2004; Funiello *et al.* 2006). Finally, the possible presence of B-type olivine fabric in the mantle wedge, which would cause fast splitting directions to be oriented perpendicular to the prevailing flow direction (Jung & Karato 2001; Karato 2003), has been explored using numerical models (Kneller *et al.* 2005, 2007).

In this study, we compare the predictions from a suite of 2-D numerical subduction zone models with shear wave splitting measurements from 17 broad-band stations in southwestern Japan. These stations, located on islands in the Ryukyu Arc and on the islands of Kyushu and southernmost Honshu, overlie the subduction of the Philippine plate beneath Eurasia. We previously examined the splitting of teleseismic shear phases at sixteen of these stations (Long & van der Hilst 2005) and noted a change from generally trench-parallel fast directions close to the trench to generally trench-perpendicular fast directions further away from the trench. We also evaluated the splitting of direct *S* phases from earthquakes originating in the Philippine slab (Long & van der Hilst 2006) and found evidence for significant trench-parallel anisotropy in the mantle wedge measured at eight stations in the Ryukyu Arc. Here, we predict shear wave splitting for a total of 460 teleseismic ray paths

and 28 local ray paths that correspond to the measurements of Long & van der Hilst (2005, 2006) and compare those predictions to the observed splitting.

We address four specific goals. First, we evaluate the effects of different rheological and thermal constraints on the flow field on simplified kinematic 2-D flow models for the Ryukyu subduction zone. Second, we calculate the distribution of finite strain, predict shear wave splitting for each of the flow models and compare the model predictions to splitting measurements due to Long & van der Hilst (2005, 2006). This allows us to evaluate how different model parameters, which affect the distribution of finite strain in the mantle wedge, affect the observable shear wave splitting. It also allows us to identify models that are most consistent with the observed shear wave splitting, which should allow us to make inferences about the style of deformation in this region. Third, we test whether a 2-D model of the flow field associated with subduction beneath southwestern Japan yields predictions that are broadly consistent with the observed splitting, which would support the use of a 2-D approximation. Finally, we briefly discuss how flow models can be integrated with an inversion of the observed splitting intensities for anisotropic structure (Long *et al.* 2007).

2 DESCRIPTION OF SPLITTING DATASET

We use data from 17 stations of the broad-band F-net array (<http://www.fnet.bosai.go.jp>); the station locations and names, along with the geometry of the subducting Philippine Sea plate from earthquake hypocentres, are shown in Fig. 1(a). Splitting parameters for

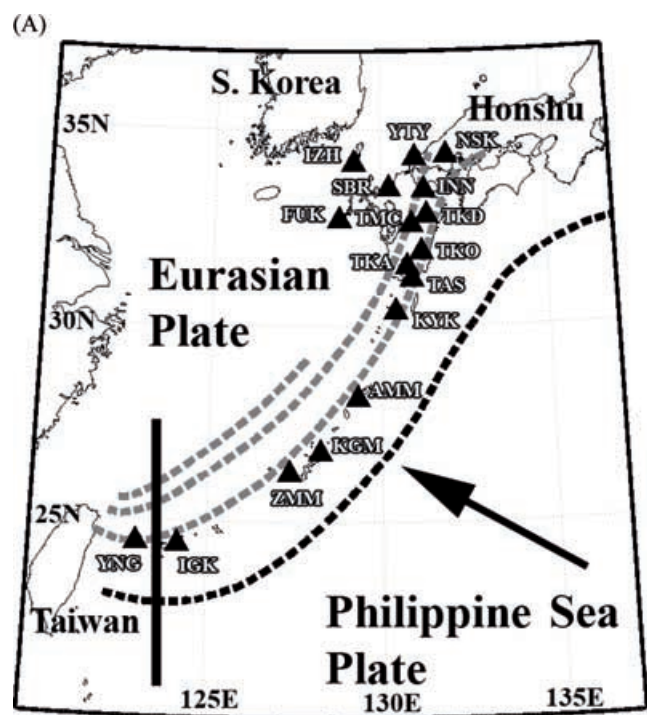


Figure 1a. Station locations and tectonic setting. Locations of the 17 broad-band F-net stations used in this study are shown as triangles. Dotted lines indicate slab contours from Gudmundsson & Sambridge (1998). The trench is shown with a black line, and slab contours at 100-km intervals are shown with grey lines. The black arrow indicates the convergence direction at the Ryukyu arc (Gripp & Gordon 2002). The location of the tomographic cross-section shown in Fig. 2a is shown as a thick black line.

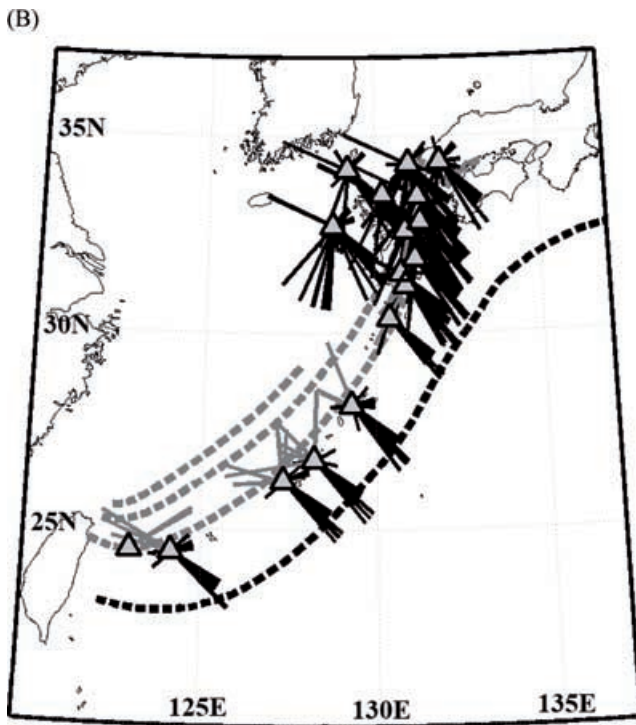


Figure 1b. Map view of ray paths for the splitting measurements used in this study. Black lines indicate the upper mantle portion of teleseismic ray paths (*SKS*, *SKKS* and direct *S*). Grey lines indicate ray paths for earthquakes originating within the Ryukyu slab.

teleseismic *SKS*, *SKKS* and direct *S* phases were measured at 16 of these stations by Long & van der Hilst (2005); splitting from local events beneath the eight southernmost stations in the array was investigated by Long & van der Hilst (2006). Ray paths for the teleseismic and local phases measured in these studies are shown in map view in Fig. 1b; Fig. 1c shows average teleseismic splitting parameters and local splitting for individual events. We note that many of the stations exhibit splitting that varies with incidence angle or backazimuth/incoming polarization azimuth, which is characteristic of underlying anisotropic structure that is more complicated than a simple, single horizontal layer of anisotropy (e.g. Silver & Savage 1994; Saltzer *et al.* 2000; Schulte-Pelkum & Blackman 2003).

Long & van der Hilst (2005, 2006) measured splitting parameters using two different techniques: the cross-correlation method used by, among others, Ando *et al.* (1983), Fukao (1984) and Levin *et al.* (1999), and the multichannel method described by Chevrot (2000). This method uses the variation in observed splitting intensity (a measure of the amount of energy observed on the transverse seismogram component) with incoming polarization azimuth to derive average shear wave splitting parameters (ϕ , δt). In this paper we use the splitting intensities measured using the Chevrot (2000) method as a basis for comparison between the model predictions and the splitting observations. For our purposes, this method has two distinct advantages: first, the splitting function (the variations in measured splitting intensities with incoming polarization azimuth) facilitates the investigation of backazimuthal variations in splitting resulting from complex anisotropic structure such as a dipping axis of symmetry or highly heterogeneous, spatially localized anisotropy. Second, the splitting intensity accrued along incremental sections of the ray path can simply be summed to predict the total intensity observed at the surface. The latter is not true in the case of the splitting param-

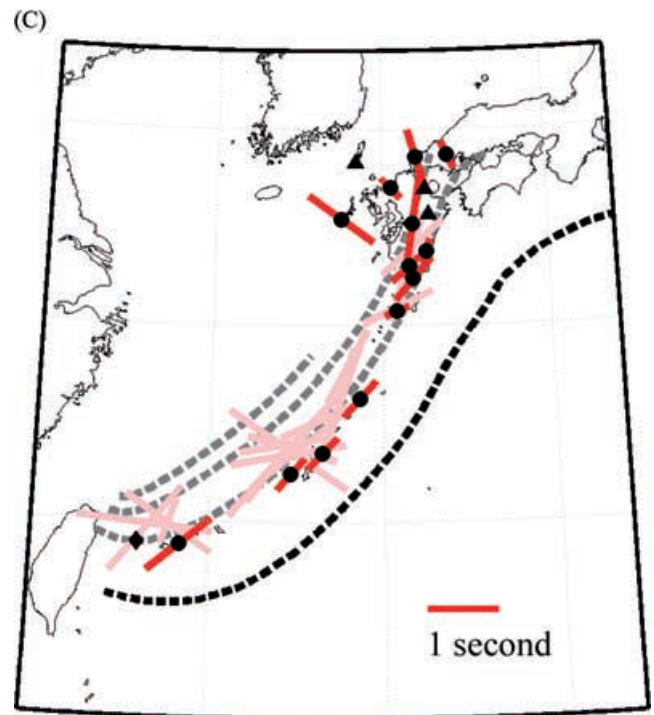


Figure 1c. Summary of measured splitting parameters from Long & van der Hilst (2005, 2006). The orientation of each bar corresponds to the fast polarization direction, and the length of each bar is scaled to the split time. Average splitting parameters for teleseismic measurements are plotted in red at the station locations (black circles). Stations with complicated teleseismic splitting patterns for which there is no physically meaningful average (Category III in Long & van der Hilst 2005) are marked with a black triangle. Teleseismic splitting was not investigated at station YNG (marked with a black diamond). Individual low-frequency local splitting measurements are plotted in pink at the midpoint of the ray.

eters (ϕ , δt) measured using the cross-correlation technique. The inverse splitting operator Γ^{-1} , which rotates and shifts the horizontal components of an individual seismogram to correct for the effect of splitting, is not commutative (Silver & Savage 1994). Therefore, the splitting intensity is a more convenient observable to work with when evaluating splitting due to complex anisotropic structures (see also Favier & Chevrot 2003; Chevrot *et al.* 2004; Favier *et al.* 2004). The splitting intensity measurement also has the advantage of dealing easily with null or near-null splitting; in this case, the splitting intensity is close to zero. In contrast, the cross-correlation method can yield inaccurate measurements when the splitting is close to null.

The most striking features of the splitting map shown in Fig. 1(c) are the preponderance of trench-parallel fast directions measured at stations located close (less than ~ 150 km) to the trench and the apparent change in orientation of the fast directions from trench-parallel to trench-perpendicular at stations located farther in the backarc. Our previous analysis (Long & van der Hilst 2006) of splitting from local events at Ryukyu Arc stations yielded fast directions and split times that were very similar to the observed teleseismic splitting, suggesting that both types of measurement reflect anisotropy in the mantle wedge above the slab. We therefore concluded (Long & van der Hilst 2006) that the most likely explanation for the observed splitting is trench-perpendicular corner flow in the mantle wedge combined with a B-type olivine fabric that results in

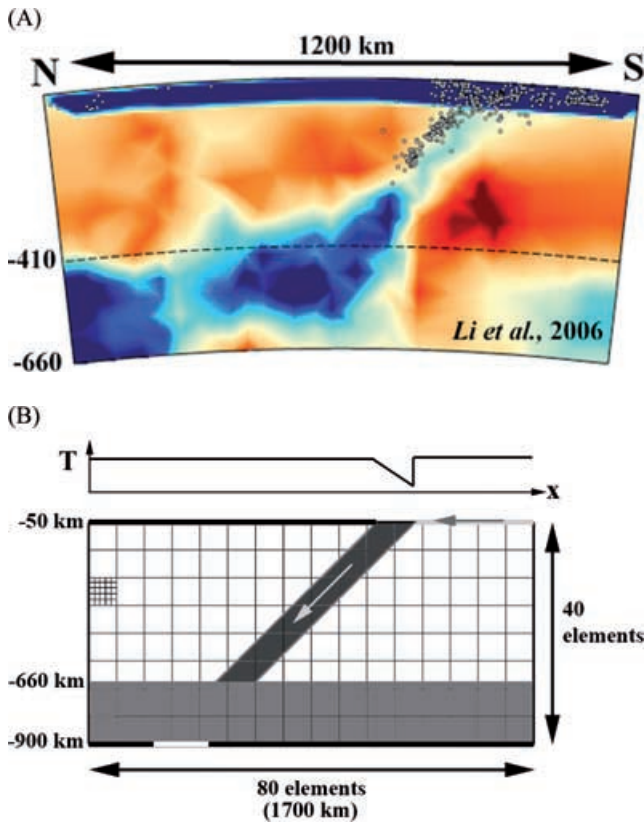


Figure 2. (a) Cross-section through the tomographic P wave speed model of Li *et al.* (2006) between the surface and the base of the transition zone. The location of the cross-section is shown on Fig. 1a. The colour bar scale ranges from +2 per cent (blue) to -2 per cent (red) perturbations to the ak135 reference model. Earthquake hypocentres from the EHB data set (Engdahl *et al.* 1998) are plotted as white circles; the dashed black line represents the 410 km discontinuity. (b) Corresponding sketch of finite element model setup. The model domain consists of 80 horizontal elements and 40 vertical elements. We model depths between 50 and 900 km, after Hall *et al.* (2000). There is no vertical exaggeration in the model and the width of the model domain is 1700 km. There is a 30-fold increase in viscosity at the 660-km discontinuity; the high-viscosity lower mantle is shown in light grey. The Ryukyu slab is modelled as a continuous, kinematically defined feature (dark grey) down to the 660 km discontinuity with a constant dip of 45° . At the top of the model domain, nodes to the left of the slab (thick black line) are pinned; nodes to the right of the slab (thick grey line) are given a constant horizontal plate velocity. Nodes within the slab are given a prescribed velocity consistent with the plate velocity at the top of the model. At the bottom of the model domain, most nodes are pinned (thick black lines), with a small section allowed to move freely (thick white line), such that material is allowed to leave the model domain. The plot at the top of the figure shows the temperature boundary condition at the top of the model domain.

a fast direction of anisotropy 90° from the prevailing flow direction (Jung & Karato 2001; Karato 2003).

Here we test such a model against the detailed splitting patterns observed at F-net stations in southwestern Japan. Our approach takes the strain field and geometry of anisotropy obtained from purely 2-D flow models. In contrast to other models that include B-type olivine fabric (Kneller *et al.* 2005, 2007), our modelling approach does not incorporate a physical basis for the B-type fabric regime; rather, we invoke a change in olivine fabric where the splitting data seem to require it. The measurements due to Long & van der Hilst (2005, 2006) are well suited to such an approach: the geographical distribution and spacing of F-net stations provide favourable ray

path coverage across much of the mantle wedge (Fig. 1b), and the good data coverage in backazimuth, incoming polarization azimuth, and incidence angle allows us to evaluate and discriminate among complex anisotropic models.

3 FLOW MODELLING FRAMEWORK

We implement a series of 2-D models for a kinematically defined downgoing slab using the ConMan finite element code (King *et al.* 1990). In the most basic model, incompressible flow in the mantle wedge is driven only by viscous coupling between the downgoing slab and the overlying mantle material. The slab dip is fixed at 45° to be roughly consistent with the geometry of the subducting Philippine Sea plate as deduced from seismicity (Engdahl *et al.* 1998; Gudmundsson & Sambridge 1999; Syracuse & Abers 2006) and seismic tomography (Nakamura *et al.* 2003; Li *et al.* 2006; see Fig. 2a). Although the dip of the Ryukyu slab is considerably less than 45° at shallow depths, we only model flow at depths greater than 50 km, where the slab is fairly well described by a constant 45° dip (Gudmundsson & Sambridge 1999). For the nodes contained within the subducting lithospheric slab, we impose kinematic velocity boundary conditions that are consistent with plate motions.

For viscous flow in an incompressible medium, the ConMan finite element code (King *et al.* 1990) solves the coupled system of equations for the conservation of momentum and energy while enforcing an incompressibility constraint using a penalty function. Following the notation of King *et al.* (1990), these equations are given by:

$$\nabla \cdot (\eta_{\text{eff}}(T, x, z) \nabla \mathbf{u}) = -\nabla P + Ra T \hat{z} \quad (1)$$

$$\nabla \cdot \mathbf{u} = 0 \quad (2)$$

$$\frac{\partial T}{\partial t} = \mathbf{u} \cdot \nabla T + \nabla^2 T, \quad (3)$$

which are the equations of conservation of momentum, mass and energy, respectively; eq. (2) enforces the incompressibility constraint. Here \mathbf{u} represents velocity, T is temperature, P is pressure (the mean of the principal stresses of the stress tensor σ_{ij}), t is time and \hat{z} is the unit vector in the vertical direction. The effective viscosity, η_{eff} , is a function of temperature and of position (x, z) . All of the dimensional material properties are combined in the non-dimensional Rayleigh number, Ra ,

$$Ra = \frac{g \alpha \Delta T d^3}{\kappa \eta_0}, \quad (4)$$

where g is the gravitational acceleration, α the thermal expansivity, ΔT the temperature drop across the model box, d the thickness of the model box, κ the thermal diffusivity and η_0 is the (dynamic) reference viscosity. All parameters are non-dimensionalized for use in the ConMan input, but hereinafter we refer to their dimensional values.

Temperature-dependent viscosity, $\eta_{\text{eff}}(T)$, is generally written in the form of the Arrhenius equation (e.g. Kohlstedt *et al.* 1995; Conrad & Hager 1999):

$$\eta_{\text{eff}}(T) = \eta_0 \exp\left(\frac{E_a}{RT} - \frac{E_a}{RT_0}\right), \quad (5)$$

where η_0 is the reference viscosity, E_a is the activation energy, T_0 is the reference temperature and R is the gas constant. We assume that viscosity is isotropic and, therefore, described by a scalar quantity, η_{eff} . Non-Newtonian rheologies are implemented in the following

manner (King & Hager 1990): the stress–strain relationship is given by

$$\dot{\varepsilon} = A \left(\frac{\sigma}{\sigma_0} \right)^n, \quad (6)$$

where $\dot{\varepsilon}$ is the second invariant of the strain-rate tensor, $\dot{\varepsilon}_{ij}$, given by $\dot{\varepsilon}_{ij} = \frac{1}{2} \left(\frac{\partial u_i}{\partial z} + \frac{\partial u_z}{\partial x} \right)$, σ is the second invariant of the stress tensor σ_{ij} , σ_0 is the reference stress and n is the power-law exponent. A is given by

$$A = \frac{\sigma_0}{\eta_0 \exp[(E_a + E_v P)/RT]}, \quad (7)$$

where E_v is the activation volume. The effective viscosity is defined by the constitutive relation for incompressible flow:

$$\eta_{\text{eff}} = \frac{\sigma}{2\dot{\varepsilon}}. \quad (8)$$

Two different forms of the effective viscosity can be defined, one based on stress and one based on strain rate:

$$\eta_{\text{eff}}^{(\text{strain rate})} = \frac{\sigma_0}{2A \frac{1}{n} \dot{\varepsilon}^{(1-\frac{1}{n})}}, \quad (9)$$

$$\eta_{\text{eff}}^{(\text{stress})} = \frac{\sigma_0^n}{2A \sigma^{(n-1)}}. \quad (10)$$

It is numerically efficient and stable to combine the two effective viscosity formulations into one geometric average, in the form given by King (1991):

$$\eta_{\text{eff}} = [\eta_{\text{eff}}^{(\text{stress})}]^x [\eta_{\text{eff}}^{(\text{strain rate})}]^{(1-x)}, \quad (11)$$

where x is a weighting factor. In our models, we use values of $n = 3$ and $x = 1/3$.

We solve this system of equations using a regular grid of 80 elements in the horizontal direction and 40 elements in the vertical direction, closely following the approach of Hall *et al.* (2000). A sketch of the model geometry is shown in Fig. 2, along with a corresponding slice through a tomographic P wave speed model for the Philippine Sea slab (Li *et al.* 2006). We model flow in the mantle between 50 and 900 km depth; each model block is 21.25 km². We impose kinematic boundary conditions consistent with the convergence speed at the Ryukyu arc (~ 50 mm yr⁻¹; Gripp & Gordon 2002) at nodes along the top right of the model box and at nodes within the 100 km thick downgoing slab. Other nodes along the top of the model domain are pinned (i.e. $u_x, u_z = 0$). Nodes along the bottom of the model domain are also pinned, except for a line of eight nodes (Fig. 2b) that allow material to leave the model domain. We define a 30-fold increase in the reference viscosity η_0 at a depth of 660 km in our models.

For models that include the effects of thermal buoyancy, we assign an isothermal boundary condition over most of the top of the model box of $T_{\text{top}} = 950$ K, which corresponds to a depth of 50 km. The temperature at the bottom, T_{bottom} , is kept at 1838 K. The initial temperature profile is defined to follow the mantle geotherm given by Stacey (1992). The incoming slab material at the top of the model domain is given a fixed temperature; this temperature increases linearly from $T_{\text{slab, left}} = 950$ K to $T_{\text{slab, right}} = 1250$ K (see Fig. 2b). This is designed to mimic the increase in temperature with depth of the lithospheric slab material as it ‘turns’ at the trench and begins its descent into the mantle. We use a thermal diffusivity $\kappa = 10^{-6}$ m s⁻² and a length scale of 1000 km. In some of our models, we implement a temperature-dependent viscosity. Following Eberle *et al.* (2002), we use values that correspond to an activation energy of ~ 500 kJ mol⁻¹, and a reference (normalizing) temperature of

1673 K; this corresponds to a decrease of four orders of magnitude in viscosity when the temperature increases from 1343 to 1673 K.

We present five models in this paper. In the most basic model, hereinafter referred to as Model A, flow is driven only by viscous coupling between the downgoing slab and the ambient mantle. In subsequent models, we add increasing complexity. Model B explores the effect on the flow pattern of adding a low-viscosity region (a viscosity reduction of two orders of magnitude) in the corner of the mantle wedge (e.g. Billen & Gurnis 2001). Model C uses a power-law rheology instead of a Newtonian (linear) rheology. With Model D we explore the effects of thermal buoyancy on the modelled flow and strain fields, and Model E illustrates the effect of a temperature-dependent viscosity law.

After obtaining steady-state velocity fields for each model, we trace streamlines through the velocity field and calculate the evolution of the finite strain along each streamline. (For the non-steady state models that include thermal buoyancy effects, we run the model for as many time steps as practical until we are as close as possible to a steady-state velocity field, and use this velocity field in subsequent calculations.) To calculate the evolution of finite strain, we follow the approach of Hall *et al.* (2000), which is based on Malvern (1969) and McKenzie (1979). In this framework, the rate of change of the finite deformation gradient tensor \mathbf{F} is defined as

$$\dot{\mathbf{F}} = \mathbf{L}\mathbf{F}, \quad (12)$$

where \mathbf{L} is the velocity gradient tensor. McKenzie (1979) gives a time-centred finite difference solution to eq. (12) in the form

$$\frac{\mathbf{F}^{n+1} - \mathbf{F}^n}{\Delta t} = \frac{\mathbf{L}(\mathbf{F}^{n+1} + \mathbf{F}^n)}{2}, \quad (13)$$

where Δt is the time increment between steps. The deformation gradient tensor is related to finite strain through:

$$\mathbf{B}^{-1} = (\mathbf{F}^{-1})^T \mathbf{F}^{-1}, \quad (14)$$

(Malvern 1969), where \mathbf{B}^{-1} is the Cauchy deformation tensor. The eigenvalues and eigenvectors of \mathbf{B}^{-1} then give us the principal axes and lengths of the 2-D strain ellipsoid; the stretch ratio of deformed length to undeformed length in the direction of the maximum strain is given by

$$r = \frac{1}{\sqrt{\lambda_{\text{max}}}}, \quad (15)$$

where λ_{max} is the eigenvalue associated with the maximum finite strain direction.

We emphasize that there are several restrictive approximations involved in our modelling approach. We assume that flow in a subduction zone is well described by a 2-D model and that the flow field is controlled by the downdip motion of the slab. We also assume that the slab is well-described everywhere by a 45° dip angle. This is a considerable simplification, as a recent global compilation of slab structure (Syracuse & Abers 2006) showed considerable along-strike complexity in the shallow structure of the Philippine Sea slab in this region, more so than in previous slab models (e.g. Gudmundsson & Sambridge 1999). Subsequent work on fully 3-D flow models for this region may clarify the relative importance of flow out of the 2-D plane considered here, but because slab roll-back is small and the slab geometry changes little along strike, we expect 3-D effects to be minor in this region. We emphasize that the objective of the work described here is to identify anisotropic models based on a 2-D approximation that are consistent with the shear wave splitting observed at the surface.

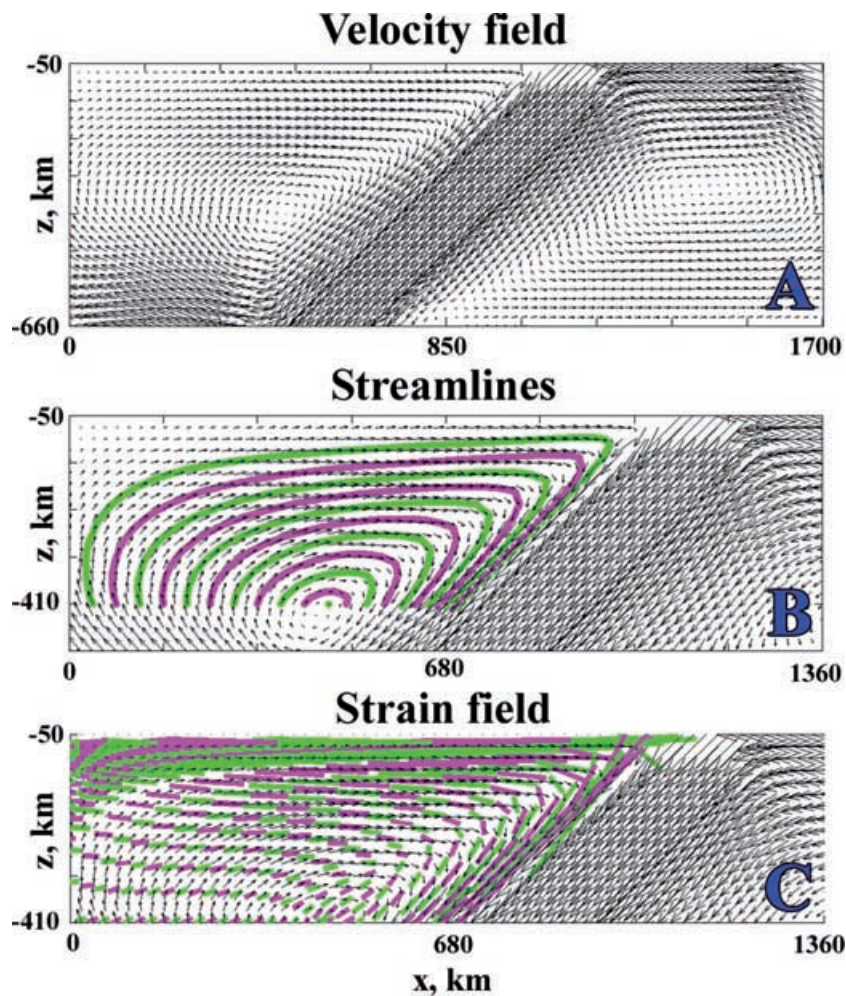


Figure 3. (a) Velocity field for the basic model setup (model A). The portion of the model corresponding to depths between 50 and 660 km is shown. Arrows correspond to velocities at individual nodes. Axis labels correspond to the depths (z) and horizontal coordinates (x) in km. (b) Streamlines traced through the velocity field displayed in (a). Alternating colours are for clarity. (c) Finite strain ellipses calculated for model A along the streamlines shown in (b). Finite strain ellipses are shown as coloured bars, with the orientation and length of the bar corresponding to the orientation and strength of the maximum finite strain direction.

4 FLOW MODELLING RESULTS: PREDICTED FLOW FIELDS

Velocity vectors, streamlines, and finite strain ellipse orientations for the simple viscous coupling model (Model A) are shown in Fig. 3. The solution for this model agrees well with models by, for example, Fischer *et al.* (2000) and Hall *et al.* (2000) and with the analytical solution for corner flow (Turcotte & Schubert 1982). For the more complex models we find differences in the details of the velocity fields and in the resulting finite strain fields. For example, Model B (with a viscosity reduction of two orders of magnitude in the corner of the wedge) and Model C (with a non-Newtonian, power-law rheology with $n = 3$) produce subtle differences in the flow field when compared with Model A. In Fig. 4, we show streamlines for Models B and C compared with the streamlines for Model A. The differences in the velocity field and streamlines are subtle for most regions of the mantle wedge but are more pronounced close to the slab (Model C) and in the wedge corner (Model B).

Model D (Fig. 5), which includes the effects of thermal buoyancy forces, produces a velocity field that is similar, but not identical to, Model A. When we add a temperature-dependent viscosity law to the model (Model E), however, a flow field is produced that is strikingly

different from that of Model D. The velocities and temperature field for Model E are shown in Fig. 6. In this model, material flows sharply upwards in the wedge corner as hot, buoyant material erodes the colder, stiffer material above it. Further away from the wedge corner, a cold, stiff layer up to ~ 100 km thick that does not participate in the flow field develops. This is similar to the behaviour observed by, for example, Eberle *et al.* (2002) for a temperature-dependent viscosity law. We calculate the evolution of the finite strain ellipse along streamlines in the mantle wedge for Models A–E; this is shown in Fig. 7. The details of the finite strain field vary from model to model, but the most dramatic change in the strain field occurs due to the temperature dependence of viscosity (i.e. model E).

In general, the different models presented in Fig. 7 do not produce large differences in the strain field, with the exception of the temperature dependent viscosity model. The addition of model features that are likely to be physically realistic (for example, a low-viscosity region in the mantle wedge corner, or a non-Newtonian rheology) do not dramatically change the modelled flow fields, again with one exception. Indeed, when constructing models for deformation in the mantle wedge above a subducting plate, uncertainties in model parameters such as using a simplified slab geometry, or using a 2-D approximation, are likely to have a larger effect on the resulting flow

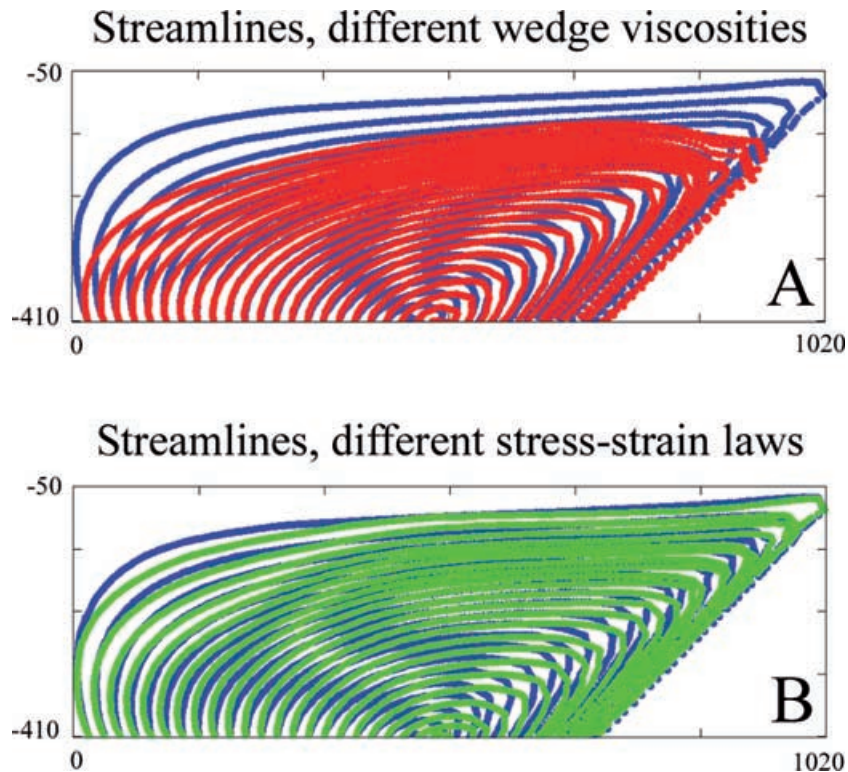


Figure 4. Streamlines for basic viscous model, a model with a low-viscosity region in the wedge corner, and a model with a non-linear ($n = 3$) rheology. (a) Streamlines for model A (blue) and model B (red) for the same starting positions. (b) Streamlines for model A (blue) and model C (green) for the same starting positions. Axis labels correspond to the depths (z) and horizontal coordinates (x) in km.

field than the use of a uniform wedge viscosity, a Newtonian rheological law, or ignoring thermal buoyancy forces. However, the use of a temperature-dependent viscosity law, which has been shown to be important in other modelling studies of convection in the mantle (e.g. Tackley 1993; Kellogg & King 1997; Zhong *et al.* 2000) and of subduction-induced flow in the mantle wedge (e.g. Eberle *et al.* 2002; Billen *et al.* 2003), does have a large effect on the velocity and finite strain fields.

5 COMPARISON OF MODEL PREDICTIONS WITH SPLITTING OBSERVATIONS FOR F-NET

In order to map the finite strain distributions into anisotropy and shear wave splitting predictions, we make additional simplifying assumptions about the relationships among strain, anisotropy and splitting. In our calculations, we follow Fischer *et al.* (2000) and Hall *et al.* (2000) and use the orientation and length in the direction of the maximum elongation of the finite strain ellipse (FSE) as a proxy for the geometry of anisotropy. The incorporation of a more detailed treatment of the development of olivine LPO into our models, such as that undertaken by Kaminski & Ribe (2001, 2002), Blackman & Kendall (2002), Kaminski *et al.* (2004) and Lassak *et al.* (2006) is beyond the scope of this paper but will be considered in future research. However, many previous studies suggest that the FSE can generally be used to infer anisotropy (e.g. Ribe 1992; Hall *et al.* 2000; Becker *et al.* 2003), although the FSE may do a poor job of approximating anisotropy in localized regions with large spatial gradients in the velocity field (Kaminski & Ribe 2002). We also assume that the observed splitting is due to anisotropy in the mantle

wedge itself; anisotropy within and beneath the slab is ignored in this treatment. This assumption is warranted on the basis of our previous work comparing local and teleseismic splitting at Ryukyu Arc stations (Long & van der Hilst 2006). We emphasize that our splitting measurements do not rule out the presence of anisotropy within the lithospheric slab or in the slab mantle, but our data do not require it, and in this study we evaluate models of wedge anisotropy that are consistent with observations.

To calculate splitting parameters from the flow models, we trace the evolution of the finite strain ellipse along streamlines throughout the mantle wedge region beginning at the base of the upper mantle ($z = 410$ km). This approach assumes that LPO development begins as material passes through the phase change in the olivine system at the 410-km discontinuity (after Hall *et al.* 2000). It is not clear, however, if the dislocation creep needed to produce olivine LPO persists to depths of 410 km (e.g. Karato 1992), and this assumption may overpredict anisotropy and splitting in the deeper part of the upper mantle. From the local FSE geometry we calculate the angle from the horizontal and the stretch ratio of maximum finite strain for each element in our model space. The distribution of stretch ratios and the dip of the FSE from the horizontal for Model A are shown in Fig. 8. We then trace rays through a ‘pseudo 3-D’ upper-mantle model for each of the 488 ray paths contained in the dataset of Long & van der Hilst (2005, 2006). Our isotropic background S wave speeds from iasp91 (Kennett & Engdahl 1991) depend only on the depth, z ; the distribution of finite strain is 2-D and depends only on depth and horizontal distance from the trench, x . The propagation of each ray, however, is calculated in three dimensions based on both the backazimuth and the ray parameter. The ray paths used in the comparison, projected into the x - z plane of the flow model, are shown in Fig. 9.

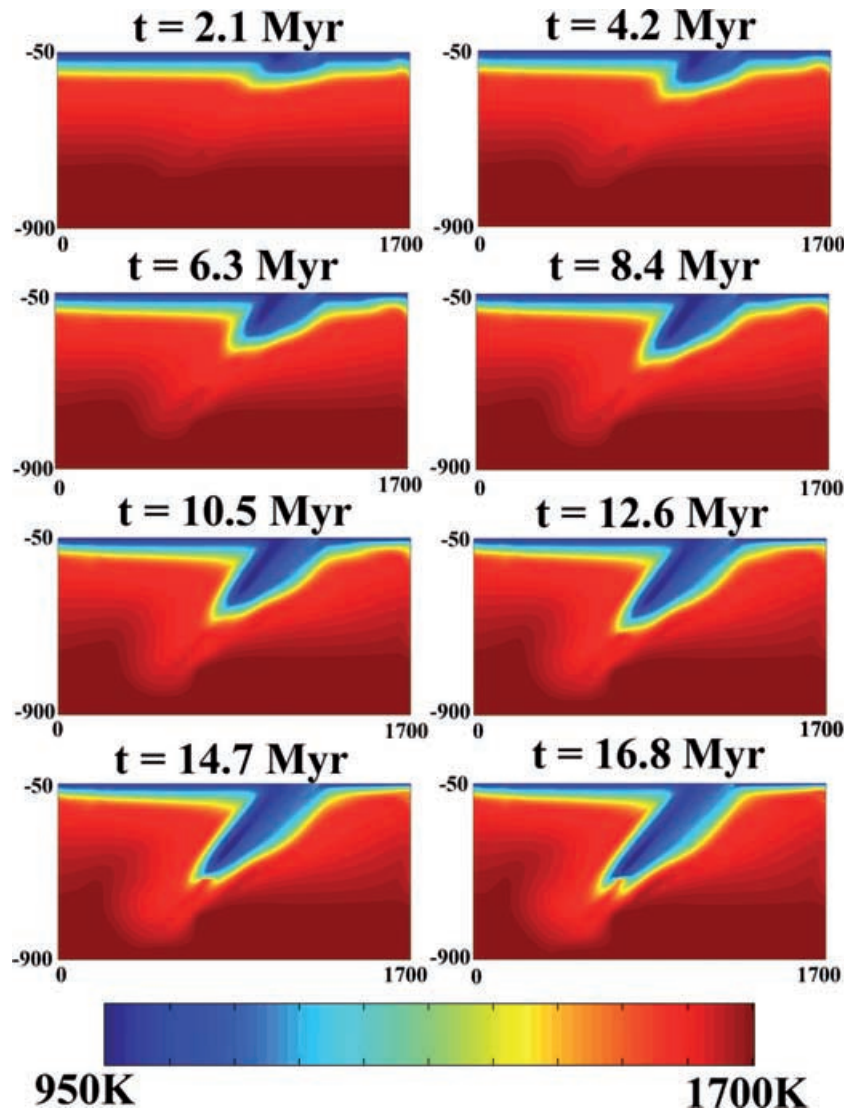


Figure 5. Time snapshots of the temperature field (colours) associated with a downgoing slab. The time-series covers approximately 17 Myr of subduction; each time step, therefore, represents about 2.1 Myr. Axis labels correspond to the depths (z) and horizontal coordinates (x) in km.

We calculate splitting in depth increments that correspond to the element size in our flow models (21.25 km). For each depth increment, we calculate the incremental splitting using the equations derived in Chevrot & van der Hilst (2003) for shear wave propagation in a transversely isotropic medium with a dipping axis of symmetry. Briefly, their approach uses anisotropic perturbation theory (after, e.g. Jech & Pšenčík 1989; Farra 2001) to derive approximate expressions for quasi-S velocities and polarizations in a weakly anisotropic medium with a dipping axis of symmetry. Chevrot & van der Hilst (2003) find that in the presence of a dipping symmetry axis, the polarizations of the quasi-S waves vary with backazimuth, with the deviation angle between the axis of symmetry and the apparent fast axis given by

$$\alpha = \arctan \left(\frac{\sin \varphi}{\frac{\tan \theta_c}{\tan \theta} - \cos \varphi} \right), \quad (16)$$

where θ_c is the angle that the symmetry axis makes with the z axis (the complement of the symmetry axis dip angle θ_0) and θ and φ are the incidence angle and azimuth, respectively, of the incoming

shear wave. The apparent fast direction for each splitting increment can, therefore, be predicted from this relation. The approximate velocities of the two quasi-S waves are given by

$$V_1 \cong \sqrt{\frac{C_{44}}{\rho}} (A_0 + A_1 \cos \varphi + A_2 \cos 2\varphi) \quad (17)$$

$$V_2 \cong \sqrt{\frac{C_{44}}{\rho}} (B_0 + B_1 \cos \varphi + B_2 \cos 2\varphi + B_3 \cos 3\varphi + B_4 \cos 4\varphi), \quad (18)$$

where ρ is the density and $A_0, A_1, A_2, B_0, B_1, B_2, B_3$ and B_4 are all functions of θ_0, θ and the elastic constants C_{ij} of the material, expressed as combinations of the Thomsen parameters ε, δ and γ (Thomsen 1986; Mensch & Rasolofosaon 1997). From these expressions, the full versions of which are given in Chevrot & van der Hilst (2003), we calculate the apparent splitting parameters φ and δt for each depth increment. We then calculate the predicted splitting intensity s for that depth increment, using (Chevrot 2000)

$$s = \delta t \sin [2(\varphi - \varphi_0)], \quad (19)$$

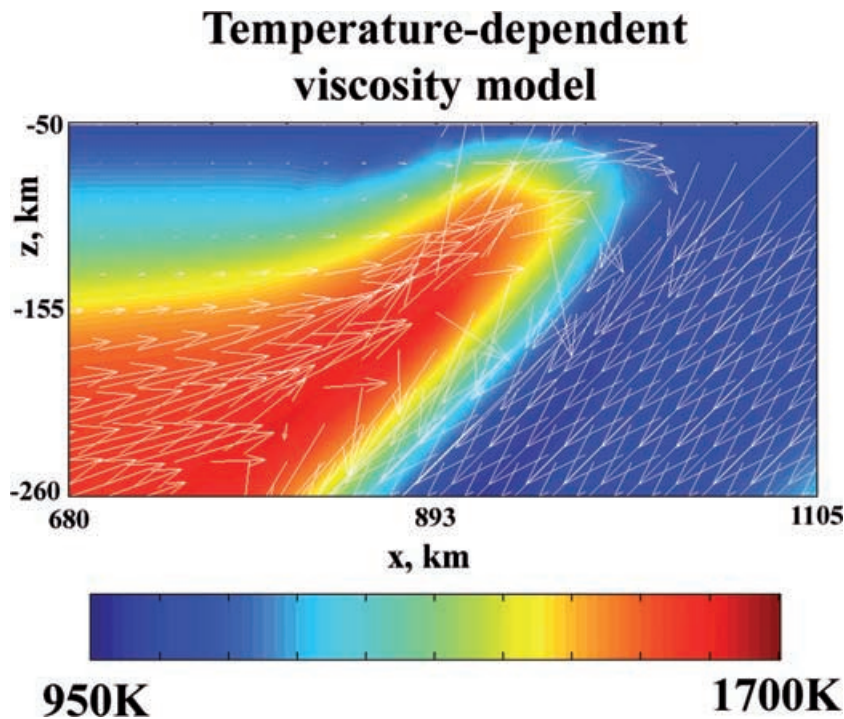


Figure 6. Temperature field (colours) and model velocities (white arrows) in the wedge corner for a model with a temperature-dependent viscosity. Axis labels correspond to the depths (z) and horizontal coordinates (x) in km.

where φ_0 is the azimuth of the apparent fast axis. Here we assume that each depth increment represents a single layer of anisotropy. The total splitting intensity for each ray path is found by summing the splitting intensities over all depth increments.

We approximate the anisotropic medium using elastic constants that are similar to those for a transversely isotropic mantle (TIM) described in Chevrot & van der Hilst (2003); a similar model was also used by Hartog & Schwartz (2000). The elastic constants were obtained by starting with the elastic tensor of single-crystal olivine (Kumazawa & Anderson 1968) and decomposing it into parts corresponding to various symmetry classes (after Browaeys & Chevrot 2004). From this decomposition, we use the isotropic and transversely isotropic parts of the tensor to obtain a TI approximation for olivine stiffness. We then mix the transversely isotropic approximation for the olivine tensor with an isotropic reference mantle of randomly oriented olivine (60 per cent) and enstatite (40 per cent), in a ratio of 1/5 (olivine) to 4/5 (isotropic mantle). This results in a TI medium with a maximum S wave anisotropy of approximately 5.9 per cent. In order to match the fairly large splitting intensities that are observed for stations that are located close to the trench and that sample a fairly small volume of mantle wedge material, we also test models using higher volumes of aligned olivine, which results in TI anisotropy of approximately 9.0 and 11.6 per cent. These elastic constants describe media similar to olivine fabrics observed in natural peridotites (Ben Ismail & Mainprice 1998) and in laboratory experiments (Zhang & Karato 1995). We then assume that the fast axis of the TIM aligns with the maximum FSE in our flow model. We further assume that once a stretch ratio of 2 has been achieved along a streamline, the LPO pattern has saturated and the splitting associated with TIM is used. This is consistent with experimental studies that show that the LPO pattern has developed to close to steady state by stretch ratios of perhaps 2–3 (e.g. Zhang & Karato 1995). For stretch ratios of less than 2, we scale the predicted split time linearly with the amount of strain; this approximates the effect

of non-steady state, weaker LPO for stretch ratios less than 2. This is a somewhat *ad hoc* representation of the development of LPO with increasing strain, but should provide a reasonable approximation of weaker LPO at smaller strains, and further work on incorporating LPO modelling into the flow models will assess the validity of this approximation.

The first thing that we would like to demonstrate with our models is that the trench-parallel splitting observations close to the trench can be reproduced with a 2-D flow model that includes a region of B-type olivine fabric. In Fig. 10 we show the data and model comparison for Model A at two selected F -net stations (AMM and TAS; see Figs 1(a) and 9 for station locations) for two cases: with and without a B-type fabric region. For the case with no B-type fabric (panels A and C in Fig. 10), the model fit is poor. This is not unexpected; the best-fitting fast directions at stations AMM, and TAS are nearly trench-parallel, and we do not expect a 2-D corner flow-type model to be able to match trench-parallel fast directions. Following the arguments in Long & van der Hilst (2006) we invoke a B-type fabric mechanism in the corner of the mantle wedge. A sketch of the ray paths that is colour-coded by the type of measurement (trench-parallel, trench-perpendicular or intermediate/complicated), shown in Fig. 11, gives us an indication of where in the model the observations require B-type fabric. We therefore, ‘flip’ the LPO, and therefore, the fast direction of anisotropy, by 90° in the horizontal plane in a triangular region extending ~ 125 km from the trench. In models that include a B-type region we recalculate the strain field and reset the accumulated strain along a streamline to zero when the streamline crosses a fabric transition, and assume that the B-type fabric develops in a similar way to A- or C-type fabric. In panels B and D of Fig. 10 we show observations and model predictions at stations AMM and TAS for the same strain model with a B-type fabric region included. The model fit improves considerably and the strain models are able to reproduce the trench-parallel splitting observations well.

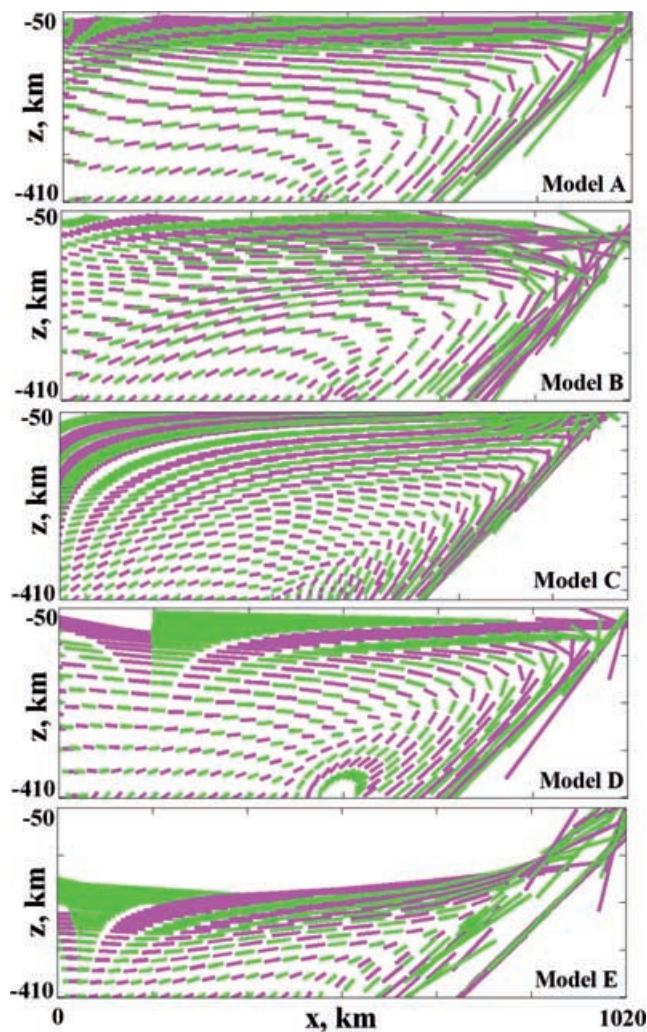


Figure 7. (a–e) Finite strain ellipses (FSE) in the mantle wedge for the models (A–E) investigated in this study. Contrasting colours are for clarity. Axis labels correspond to the depths (z) and horizontal coordinates (x) in km.

In Fig. 12 we show the splitting measurements and model predictions for four F-net stations (AMM, NSK, SBR and FUK; see station locations in Figs 1a and 9) at increasing distances from the trench for the strain field derived from Model A, with a B-type fabric region in the mantle wedge. To obtain the splitting predictions shown we used anisotropic media with maximum anisotropy of 9.0 per cent in the B-type region and 5.7 per cent in the rest of the model. In general, the qualitative features of the splitting patterns are reproduced well by the strain model, although at most stations there are several individual splitting intensity measurements that are not well matched by the predictions. When we examine the predictions for Model E, which produces a strain field that is markedly different from Model A, we find that the detailed splitting patterns at most stations are also substantially different. Fig. 13 shows the observed and predicted splitting at the same four stations with the same elasticity models for Model E, modified to include the same B-type region in the wedge corner. We find that details of the splitting predictions are different at several of the stations, and the fit to the measured splitting is often better. However, for stations that sample mostly B-type fabric in the mantle wedge, such as station AMM in Figs 12 and 13, the strain model does not have a large

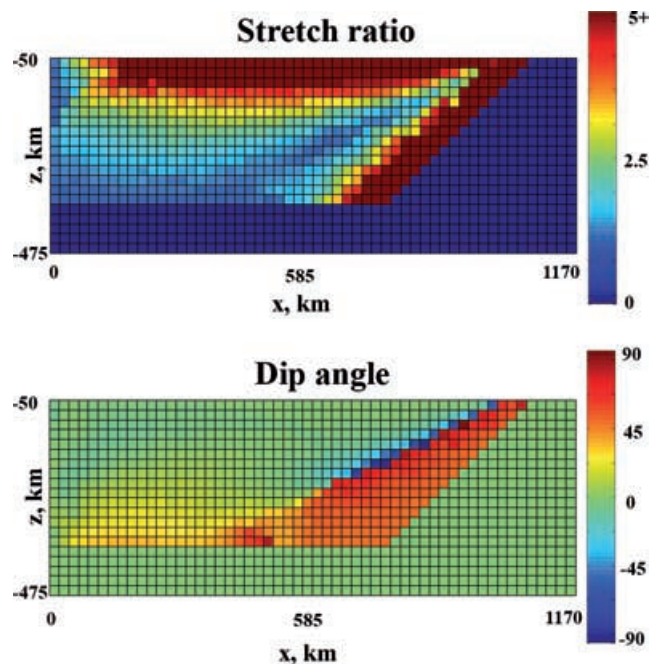


Figure 8. (a) Colour representation of the magnitude of the maximum finite strain field for Model A. Colour bar goes from stretch ratios of 0 (blue) to stretch ratios of 5 or greater (red). (b) Colour representation of the angle of the maximum finite strain ellipse with the horizontal for Model A. Near-horizontal angles are shown in green; the colour scale goes from angles of 90° counter-clockwise from horizontal (red) to 90° clockwise from horizontal (blue). Axis labels correspond to the depths (z) and horizontal coordinates (x) in km.

effect on the predicted splitting. This is due to the rotation of the fast direction 90° from the flow direction in the shear plane, which results in a horizontal trench-parallel fast axis regardless of the local dip of the finite strain ellipse in the strain model. This demonstrates the importance of using splitting observations from stations that sample the region dominated by A- or C-type olivine fabric in order to constrain the rheological parameters controlling the mantle flow.

We emphasize that (for stations located more than ~ 100 km from the trench which sample the A-/C-type fabric regime) the visual character of the splitting patterns is not drastically different for different strain models, and the *average* splitting parameters (φ , δt) that we would predict at each station are not much different from those for Model A versus Model E (Figs 12 and 13). These observations are borne out when we examine the model predictions at, as an example, station SBR for four different flow models (Fig. 14). Here we show predictions for Models A, B, D and E; Model C is not shown in this figure because of its close similarity with Model A. All of the model predictions fit the observations fairly well, but the details of the splitting patterns for different models are substantially different. This suggests that the *average* shear wave splitting observed at the surface, while generally consistent with the predictions of our flow models, is not very sensitive to the details of the model parameters used. Vice versa, the average of the measured splitting parameters is not sensitive to rheological properties in the mantle wedge. However, because the detailed predicted splitting patterns at each station are substantially different for different models, a dense dataset with good sampling at individual stations (such as that of Long & van der Hilst 2005, 2006) could be used to constrain the pattern of anisotropy of the wedge, and therefore, to the rheological properties that control it. This gives us confidence

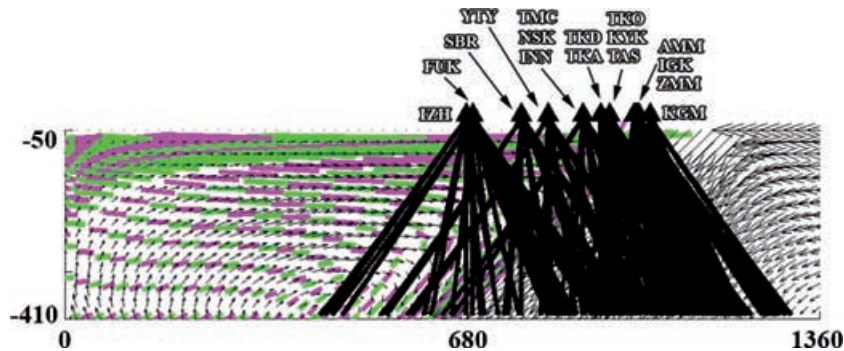


Figure 9. Sketch of ray paths in the splitting dataset projected onto the 2-D model plane. The distribution of finite strain in the wedge for Model A is shown. Station locations are marked with a black triangle and station names are shown.

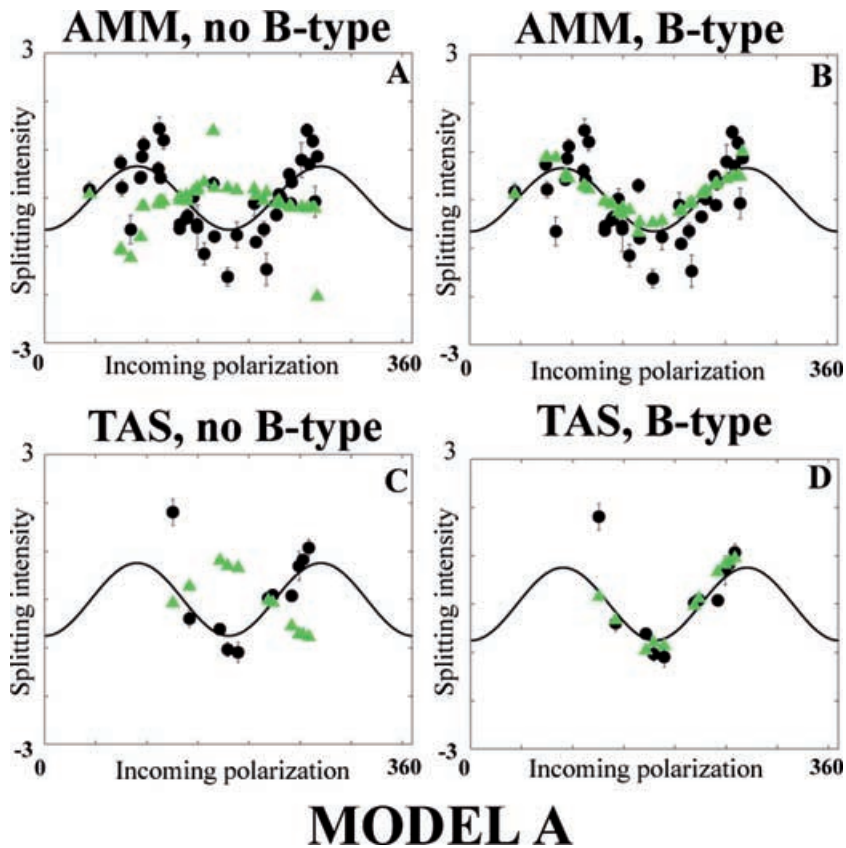


Figure 10. (a–d) Comparison of splitting observations (black circles) and model predictions (green triangles) for Model A with and without a B-type fabric region at stations AMM and TAS. The best-fitting $\sin(2\theta)$ curve to the observed splitting is shown in black. Splitting intensities (y -axis) are plotted with respect to incoming polarization azimuths (x -axis). Both stations are located fairly close to the trench (see Fig. 9); the model that includes B-type fabric produces noticeably better fits to the observations. The B-type fabric region is modelled with elastic constants corresponding to a medium with a maximum of 9.0 per cent shear wave anisotropy.

that we can interpret the detailed splitting patterns we observe in southwestern Japan in terms of the 2-D anisotropic geometry in the mantle wedge.

6 DISCUSSION

We have tested predictions from several flow models against the observed splitting data. We find that B-type fabric (Jung & Karato 2001; Karato 2003) or a similar mechanism such as melt-influenced LPO (Holtzmann *et al.* 2003) is needed to reconcile the trench-parallel fast directions that we observe in southwestern Japan with

a 2-D flow model. There are several issues, however. First, our 2-D flow modelling approach ignores the possible effects of flow around the slab edge or flow induced by effects such as slab rollback or backarc extension. Because the rollback rate of the Ryukyu trench is slow compared to the downdip motion of the slab (Heuret & Lallemand 2005, and references therein; Lallemand *et al.* 2005), we have previously argued (Long & van der Hilst 2006) that the flow field is likely dominated by convergence-parallel flow and that 3-D flow effects are probably small. Second, there are outstanding questions about the applicability of B-type fabrics observed in the laboratory to the Earth's mantle; studies have questioned

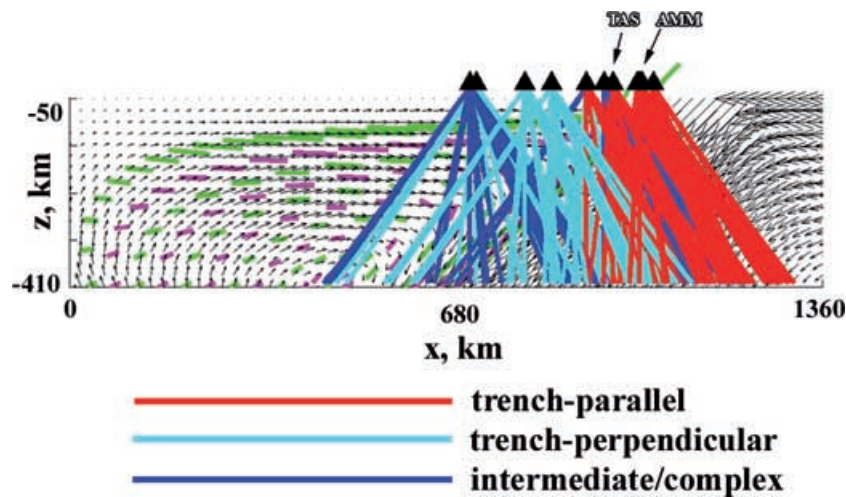


Figure 11. Cross-sectional plot of all teleseismic ray paths in this study, colour-coded by type of observation. Rays associated with near trench-parallel fast directions are shown in red; rays associated with near trench-perpendicular fast directions are shown in light blue. Rays associated with stations for which the measured splitting is complex (Category III stations in Long & van der Hilst 2005) are shown in dark blue. The velocity vectors and finite strain distribution for Model A are shown. Axis labels correspond to the depths (z) and horizontal coordinates (x) in km. For reference, the locations of stations AMM, FUK, IGK and TAS (Fig. 10) are shown.

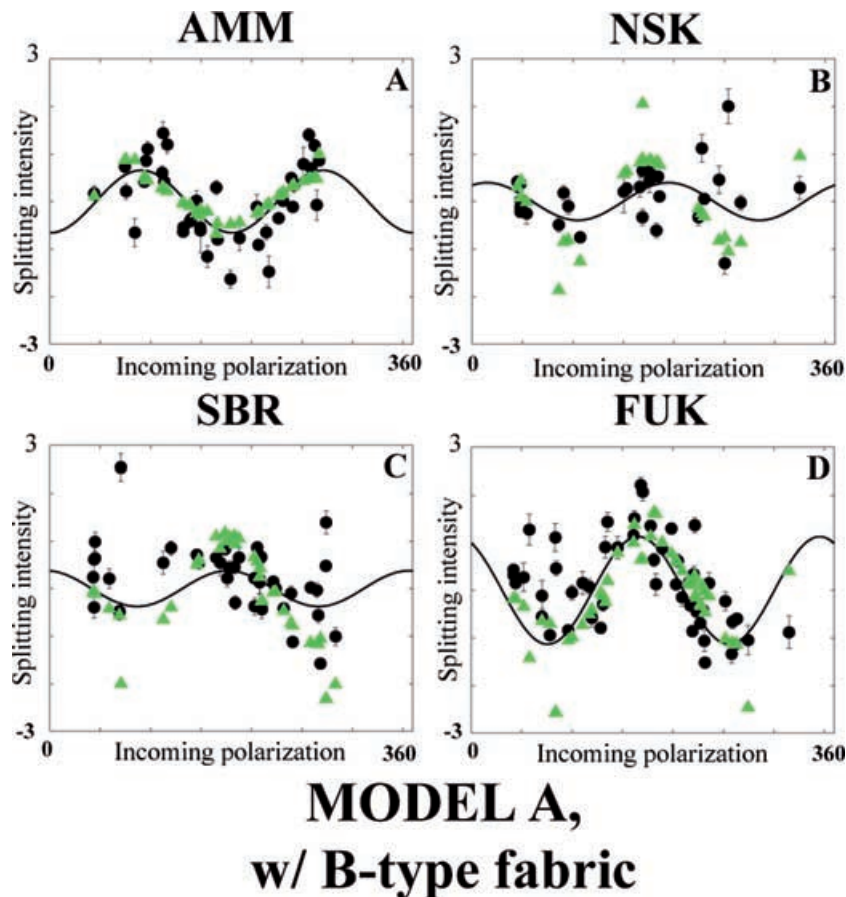


Figure 12. (a–d) Comparison of splitting observations (black circles) and model predictions (green triangles) for Model A (includes a region dominated by B-type fabric) at four stations (AMM, NSK, SBR and FUK). The stations are arranged in order of increasing distance from the trench, from AMM (panel A) to FUK (panel D). The best-fitting $\sin(2\theta)$ curve to the observed splitting is shown in black. Splitting intensities (y -axis) are plotted with respect to incoming polarization azimuths (x -axis).

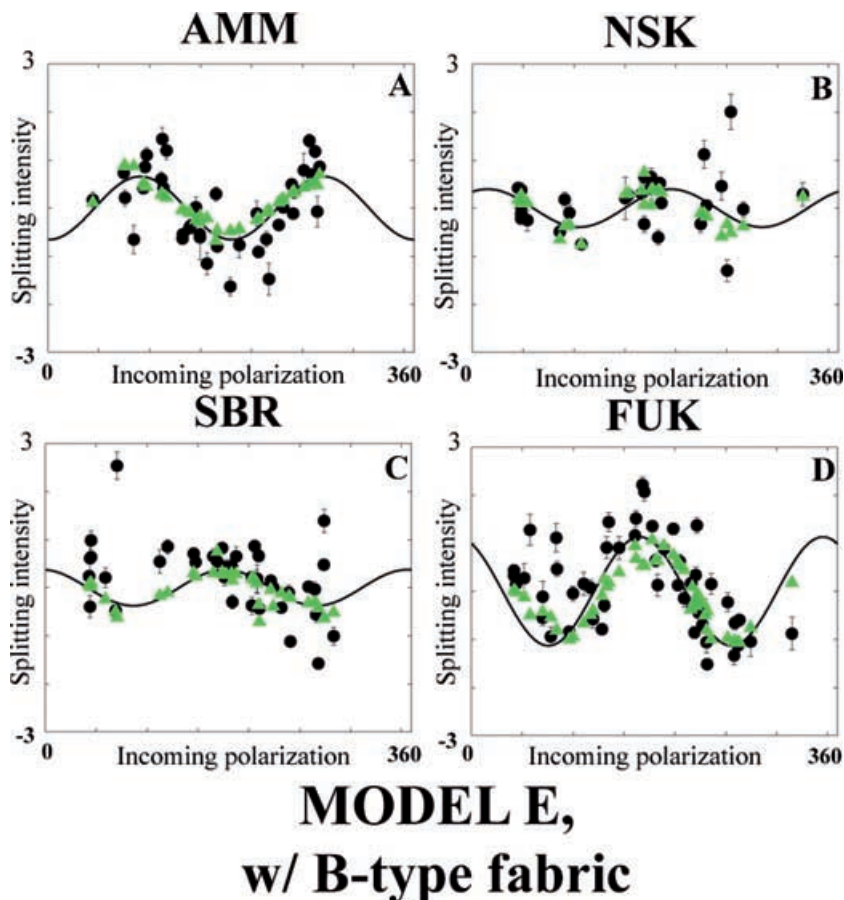


Figure 13. (a–d) Comparison of splitting observations (black circles) and model predictions (green triangles) for Model E (includes a region dominated by B-type fabric) at four stations (AMM, NSK, SBR and FUK). The stations are arranged as in Fig. 12. The best-fitting $\sin(2\theta)$ curve to the observed splitting is shown in black. Splitting intensities (y -axis) are plotted with respect to incoming polarization azimuths (x -axis).

whether the physical and chemical conditions needed to produce B-type fabric are present in large volumes of the mantle wedge (e.g. Kaminski 2002). However, recent (Kneller *et al.* 2005, 2007) and ongoing modelling studies are examining in detail whether the stress, strain and hydration conditions needed to produce B-type fabric are in fact achieved in large portions of the wedge corner. There is a growing body of evidence from experimental (Jung & Karato 2001; Katayama & Karato 2007), petrographic (Mizukami *et al.* 2004; Katayama *et al.* 2005; Skemer *et al.* 2006), observational (Nakajima & Hasegawa 2004; Long & van der Hilst 2006; Nakajima *et al.* 2006) and modelling (Lassak *et al.* 2006; Kneller *et al.* 2006) studies that B-type fabric may indeed be important (and observable) in certain regions of the mantle wedge.

The approach we have taken to modelling anisotropy and splitting in this paper contains several approximations; in particular, we do not model the development of LPO *per se*, but use the orientation of the finite strain axis along with reasonable elastic constants as a proxy for LPO. This assumption ignores the ‘lag’ in LPO development in regions where the velocity field changes rapidly (e.g. Kaminski & Ribe 2002) and also ignores the effects of LPO reorganization when a streamline crosses a fabric transition. It is important to appreciate, therefore, that in regions of the model where velocity changes over short length scales or where material undergoes a transition from A-/C-type fabric to B-type fabric (or vice versa), our splitting predictions may be inadequate. Indeed, there is some suggestion from our modelling that we fit the splitting observations

less well at stations that may sample the fabric transition (e.g. station NSK, as opposed to stations AMM and FUK, in Figs 12 and 13). Further characterization of these effects should be possible on two fronts: through the integration of LPO modelling (e.g. Kaminski *et al.* 2004) with the models described in this study, and/or through the implementation of an inverse problem approach (e.g. Chevrot 2006, Long *et al.* 2007).

We emphasize that the approach we have taken to identifying the region dominated by B-type fabric is driven by the splitting observations; we do not attempt to predict the B-type fabric region, and our models do not contain or describe the ‘physics’ of the olivine fabric transition. A complementary approach is taken by Kneller *et al.* (2005, 2007); their models incorporate laboratory results for olivine rheology (Katayama & Karato 2007) and LPO development (Jung & Karato 2001; Katayama *et al.* 2004) and predict the region of the wedge in which the B-type fabric should dominate. Some of the physical conditions of our models are inconsistent with predictions from these models of B-type fabric, which include a region of slow flow in the cold, high-stress nose of the mantle wedge where finite strain accumulates relatively slowly (Kneller *et al.* 2005, 2007). However, many of the characteristics of the finite strain field predicted by these B-type fabric models and our models, where the B-type region is inserted according to where the observations seem to require it, are generally quite similar. We are currently undertaking a detailed comparison of our splitting dataset with models that predict the B-type fabric region and preliminary work indicates that

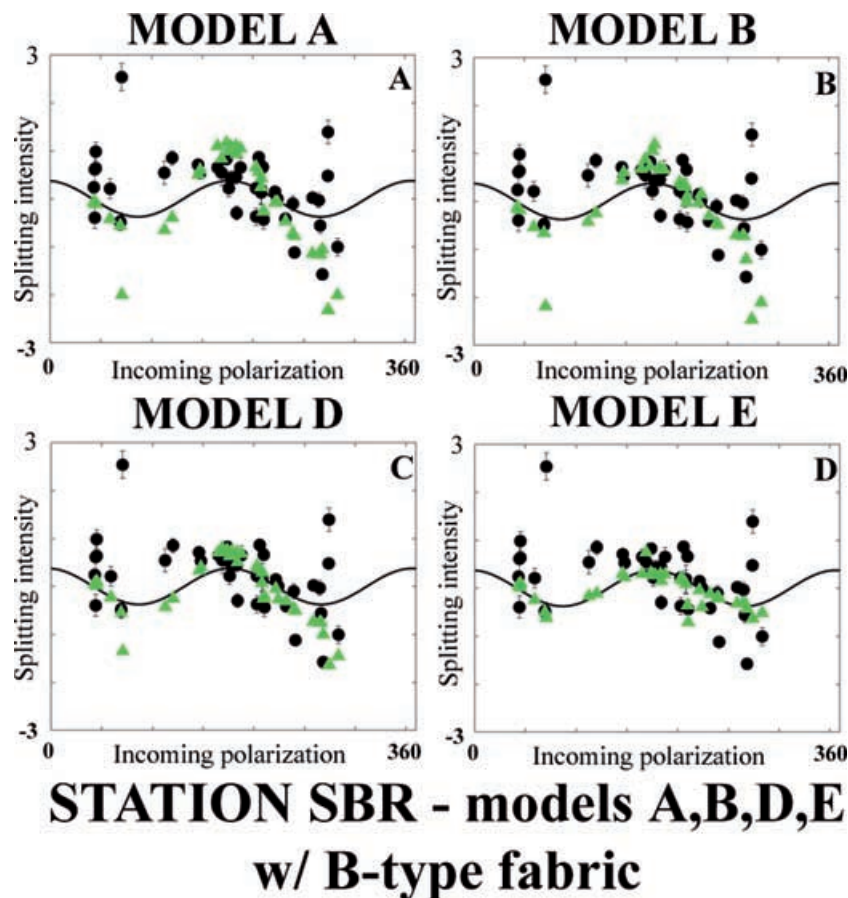


Figure 14. (a–d) Comparison of splitting observations (black circles) and model predictions (green triangles) for four models (Models A, B, D and E) at station SBR. The strain distribution for Model C is very similar to that of Model A and is, therefore, not shown in this figure. Splitting intensities (y -axis) are plotted with respect to incoming polarization azimuths (x -axis).

the results we obtain with our more observation-driven approach are consistent with such models (Kneller *et al.* 2006). One important preliminary result of this comparison is that the amount of splitting that can be produced by a B-type fabric region is very sensitive to the details of the slab geometry at each station, particularly the shallow slab structure (Syracuse & Abers 2006; Kneller *et al.* 2006). It is important to keep in mind that the study described in this paper uses a simplified slab geometry that is assumed to be constant everywhere along the strike of the trench; further work such as that described by Kneller *et al.* (2006) is needed to fully characterize the importance of shallow slab structure and along-strike variations in slab morphology.

The good match produced by the models presented here supports the hypothesis (Long & van der Hilst 2006) that the observed splitting can be produced with a 2-D model that invokes trench-perpendicular flow coupled to the downdip motion of the slab with a region of B-type olivine fabric in the corner of the wedge. However, the models considered here are unable to match every detail of the splitting patterns observed at each of the 17 stations examined. Part of this mismatch may be due to along-strike variations in slab geometry, flow field, and the resulting anisotropy. However, much of the mismatch between the observed and predicted splitting is likely due to incorrect or inadequate aspects of the 2-D forward models themselves. Our forward modelling approach can help identify geodynamically plausible models that are consistent with the observations, but without a comprehensive search of the parameter space

(which is impractical) it is not clear how unique such solutions are. In particular, our approach to modelling predicted splitting intensities suffers from trade-offs between the geometry of anisotropy derived from the finite strain field and the strength of anisotropy (that is, the elasticity tensor) that is used. Our study not only illustrates the potential for using observations of splitting intensity at station located above subduction zones to discriminate among different reholological models, it also illustrates the limitations of a forward modelling approach. Moving to an inverse problem approach such as that outlined by Chevrot (2006) and Long *et al.* (2007) should allow us to refine the results presented here and identify a 2-D anisotropic model that best fits the observed splitting. In a future study, the models produced here will be used as starting models in a formal inversion approach, in which we invert the mismatch between observed and predicted splitting intensities for an updated 2-D anisotropic structure; this work is currently in progress. One goal of this inversion approach is to identify appropriate flow modelling ‘control parameters’ that come closest to matching the strain geometry we retrieve from (well-resolved areas of) the splitting inversion. For example, an inversion approach could identify best-fitting values for the activation energy E_a in the temperature-dependent viscosity law, the power n in the non-Newtonian rheology law, or the stress or strain rate below which the rheology becomes Newtonian and LPO does not develop.

As we have discussed, there are strong trade-offs between finite strain geometry and the strength of the anisotropic media used to

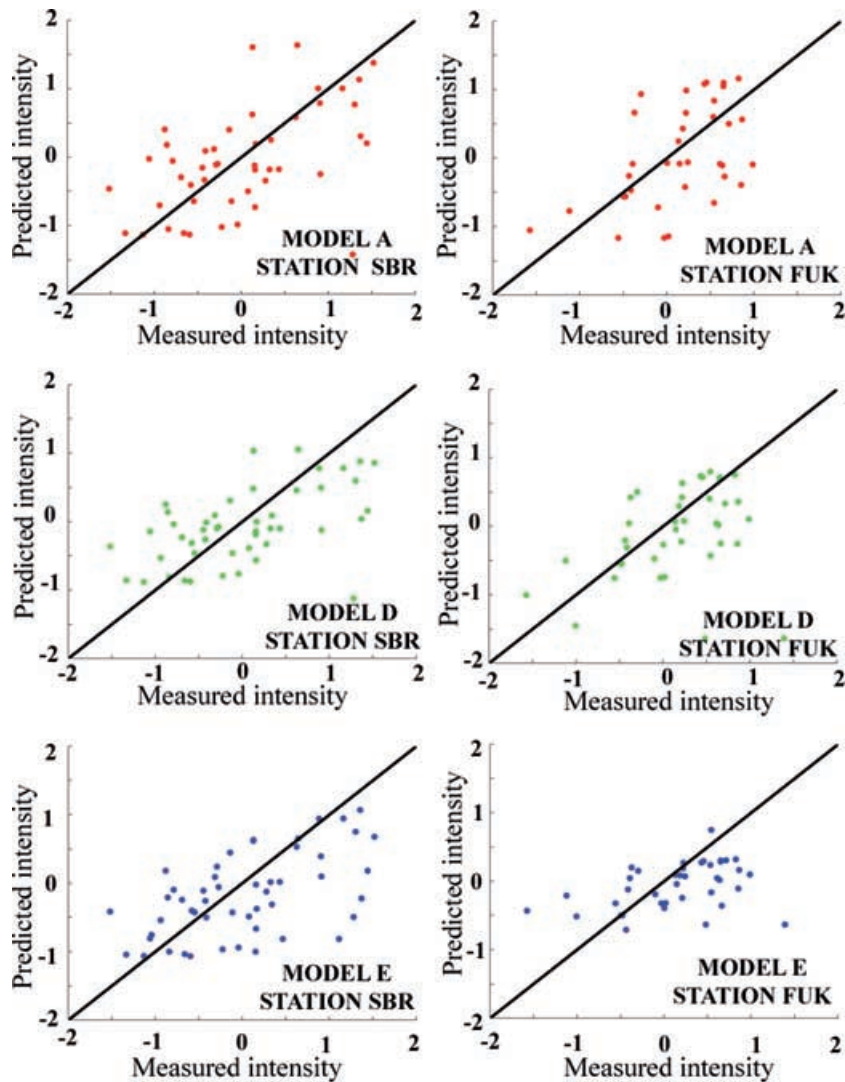


Figure 15. Scatter plots comparing observed (x -axis) and predicted (y -axis) values of splitting intensity at stations SBR (left-hand panels) and FUK (right-hand panels) for the three different strain models (A, B and E) that produce the most dramatically different splitting predictions. Each strain model contains a region dominated by B-type olivine fabric.

model the splitting intensity. Because of these trade-offs, it is difficult to settle on a ‘preferred’ rheological model using only a forward modelling approach. However, we have compared the model fits to the data by calculating a χ^2 statistic for the entire splitting data set for each model. We have also visually examined scatter plots for individual stations for different strain models and different anisotropy strengths; examples of such plots for two stations (SBR and FUK) are shown in Fig. 15. We can also, of course, visually evaluate the different model fits by looking at observed and predicted splitting patterns for individual stations, such as those shown in Figs 12–14. The χ^2 statistic, which measures the discrepancy between the observed and predicted splitting intensity values, is expressed as $\chi^2 = \sum_{\text{all}} (s_{\text{obs}} - s_{\text{predicted}})^2$. We have computed χ^2 values for both the entire dataset and for individual stations (see the examples in Fig. 15) for Models A–E. In this calculation, we assumed a maximum anisotropy strength of 9.0 per cent in the B-type fabric region and 5.7 per cent elsewhere in the model. We found that the χ^2 values for Models A–E, respectively, are 397.7, 382.3, 423.2, 331.6 and 241.8. Model E, therefore, provides the best fit to the splitting data set, followed by Model D. With the caveat that this

reduction in χ^2 cannot be taken quite at face value because of the trade-off between the geometry and strength of anisotropy, this result may underscore the importance of thermal buoyancy effects in the modelling of subduction zone anisotropy. The law for temperature dependent viscosity used in Model E is likely to be more physically realistic (e.g. Kelemen *et al.* 2003), and the high temperatures in the shallow regions of the wedge corner predicted by this and similar models is perhaps more consistent with petrologic evidence (Elkins Tanton *et al.* 2001). However, it is not clear if the temperatures in this particular model are consistent with the conditions needed to sustain B-type olivine fabric (Kneller *et al.* 2005, 2007). In any case, the direct inversion of our shear wave splitting data set should provide tighter constraints on the geometry and strength of anisotropy than can be provided by forward modelling alone, and this work should help to discriminate further among the possible models. The forward modelling discussed in this paper demonstrates that changes in 2-D finite strain distribution and changes in the elastic constants used to model anisotropy do manifest themselves in changes in shear wave splitting intensity that can be observed at the surface.

8 CONCLUSIONS

We have computed velocity and finite strain fields for a suite of 2-D numerical models of flow in the mantle wedge associated with a downgoing slab. Combining these models with assumptions about the relationship between maximum finite strain and the resulting anisotropy allows us to predict shear wave splitting. We have applied this technique to southwestern Japan, using flow model boundary conditions appropriate for the subduction of the Philippine Sea plate beneath Eurasia and comparing the model splitting predictions to a shear wave splitting dataset for seventeen broad-band stations located in the Ryukyu Arc, Kyushu and southernmost Honshu. We draw the following conclusions: (1) We are able to identify flow models that are consistent with the observed splitting, which suggests that the 2-D approximation for the flow field is reasonable. (2) The splitting intensity introduced by Chevrot (2000) provides a natural and visually intuitive way of comparing splitting observations with the model predictions. (3) The *average* predicted splitting parameters are relatively insensitive to the details of the finite strain field, and therefore, to the parameters used in the flow models. However, the details of the splitting patterns predicted for different models are dramatically different. This suggests that a rigorous analysis of the details of splitting patterns for dense splitting datasets, such as the dataset of Long & van der Hilst (2005, 2006), can discriminate among different rheological models for flow in the mantle wedge. (4) Our data require a region of B-type olivine fabric in the wedge corner, extending ~ 125 km into the backarc. This is consistent with other, complementary modelling studies of B-type fabric in the mantle wedge (e.g. Kneller *et al.* 2005, 2006, 2007). (5) The flow modelling framework presented here yields starting models that are suitable for the tomographic inversion of splitting intensity measurements for anisotropic structure, which may constrain appropriate values for flow modelling control parameters such as activation energy.

ACKNOWLEDGMENTS

We thank Tim Grove, Shun Karato, Erik Kneller, Stéphane Rondenay and Peter van Keken for helpful comments and discussions, and Einat Lev, Erwan Mazarico and James Dennedy-Frank for their assistance with the ConMan software. Fig. 2(a) was provided by Chang Li. We thank Editor Hans-Joachim Kuempel and Karen Fischer for helpful comments that improved the manuscript. F-net data are collected and disseminated by the Japanese National Research Institute for Earth Science and Disaster Prevention (NIED). This work was supported by NSF grant EAR-0337697.

REFERENCES

- Anderson, M.L., Zandt, G., Triep, E., Fouch, M. & Beck S., 2004. Anisotropy and mantle flow in the Chile-Argentina subduction zone from shear wave splitting analysis, *Geophys. Res. Lett.*, **31**, doi:10.1029/2004GL020906.
- Ando, M., Ishikawa Y. & Yamazaki, F., 1983. Shear wave polarization anisotropy in the upper mantle beneath Honshu, Japan, *J. geophys. Res.*, **88**, 5850–5864.
- Anglin, D.K. & Fouch, M.J., 2005. Seismic anisotropy in the Izu-Bonin subduction system, *Geophys. Res. Lett.*, **32**, doi:10.1029/2005GL022714.
- Arcay, D., Tric, E. & Doin, M.P., 2005. Numerical simulations of subduction zones: effect of slab dehydration on the mantle wedge dynamics, *Phys. Earth Planet. Inter.*, **149**, 133–153.
- Becker, T.W., Kellogg, J.B., Ekstrom, G. & O'Connell, R.J., 2003. Comparison of azimuthal seismic anisotropy from surface waves and finite strain from global mantle-circulation models, *Geophys. J. Int.*, **155**, 696–714.
- Behn, M.D., Conrad, C.P. & Silver, P.G., 2004. Detection of upper mantle flow associated with the African Superplume, *Earth planet. Sci. Lett.*, **224**, 259–274.
- Ben Ismaïl, W. & Mainprice, D., 1998. An olivine fabric database: an overview of upper mantle fabrics and seismic anisotropy, *Tectonophysics*, **296**, 145–157.
- Billen, M.I. & Gurnis, M., 2001. A low viscosity wedge in subduction zones, *Earth planet. Sci. Lett.*, **193**, 227–236.
- Billen, M.I., Gurnis, M. & Simons, M., 2003. Multiscale dynamics of the Tonga-Kermadec subduction zone, *Geophys. J. Int.*, **153**, 359–388.
- Blackman, D. & Kendall, J.-M., 2002. Seismic anisotropy in the upper mantle 2. Predictions for current plate boundary flow models, *Geochem. Geophys. Geosyst.*, **3**, doi:10.1029/2001GC000247.
- Browaays, J.T. & Chevrot, S., 2004. Decomposition of the elastic tensor and geophysical applications, *Geophys. J. Int.*, **159**, 667–678.
- Buttles, J. & Olson, P., 1998. A laboratory model of subduction zone anisotropy, *Earth planet. Sci. Lett.*, **164**, 245–262.
- Chevrot, S., 2000. Multichannel analysis of shear wave splitting, *J. geophys. Res.*, **105**, 21 579–21 590.
- Chevrot, S., 2006. Finite-frequency vectorial tomography: a new method for high-resolution imaging of upper mantle anisotropy, *Geophys. J. Int.*, **165**, 641–657.
- Chevrot, S. & Van Der Hilst, R.D., 2003. On the effects of a dipping axis of symmetry on shear wave splitting measurements in a transversely isotropic medium, *Geophys. J. Int.*, **152**, 497–505.
- Chevrot, S., Favier, N. & Komatitsch, D., 2004. Shear wave splitting in three-dimensional anisotropic media, *Geophys. J. Int.*, **159**, 711–720.
- Conder, J.A., Wiens, D.A. & Morris, J., 2002. On the decompression melting structure at volcanic arcs and back-arc spreading centers, *Geophys. Res. Lett.*, **29**, doi:10.1029/2002GL015390.
- Conrad, C.P. & Hager, B.H., 1999. Effects of plate bending and fault strength at subduction zones on plate dynamics, *J. geophys. Res.*, **104**, 17 551–17 571.
- Currie, C.A., Cassidy, J. F., Hyndman, R.D. & Bostock, M. G., 2004. Shear wave anisotropy beneath the Cascadia subduction zone and western North American craton, *Geophys. J. Int.*, **157**, 341–353.
- Eberle, M.A., Grasset, O. & Sotin, C., 2002. A numerical study of the interaction of the mantle wedge, subducting slab, and overriding plate, *Phys. Earth planet. Inter.*, **134**, 191–202.
- Elkins Tanton, L.T., Grove, T. L. & Donnelly-Nolan, J., 2001. Hot, shallow melting under the Cascades volcanic arc, *Geology*, **29**, 631–634.
- Engdahl, E.R., Van Der Hilst, R.D. & Buland, R.P., 1998. Global teleseismic earthquake relocation from improved travel times and procedures for depth determination, *Bull. seism. Soc. Am.*, **88**, 722–743.
- Farra, V., 2001. High order perturbations of the phase velocity and polarization of *qP* and *qS* waves in anisotropic media, *Geophys. J. Int.*, **147**, 93–104.
- Favier, N. & Chevrot, S., 2003. Sensitivity kernels for shear wave splitting in transverse isotropic media, *Geophys. J. Int.*, **153**, 213–228.
- Favier, N., Chevrot, S. & Komatitsch, D., 2004. Near-field influences on shear wave splitting and traveltimes sensitivity kernels, *Geophys. J. Int.*, **156**, 467–4482.
- Fischer, K.M. & Yang, X., 1994. Anisotropy in Kuril-Kamchatka subduction zone structure, *Geophys. Res. Lett.*, **21**, 5–8.
- Fischer, K.M., Fouch, M. J., Wiens, D.A. & Boettcher, M. S., 1998. Anisotropy and flow in Pacific subduction zone back-arcs, *Pure appl. Geophys.*, **151**, 463–475.
- Fischer, K.M., Parmentier, E.M., Stine, A.R. & Wolf, E.R., 2000. Modeling anisotropy and plate-driven flow in the Tonga subduction zone back arc, *J. geophys. Res.*, **105**, 16 181–16 191.
- Fukao, Y., 1984. Evidence from core-reflected shear waves for anisotropy in the Earth's mantle, *Nature*, **309**, 695–698.
- Funiciello, F., Faccenna, C., Giardini, D. & Regenauer-Lieb, K., 2003. Dynamics of retreating slabs: 2. Insights from 3-D laboratory experiments, *J. geophys. Res.*, **108**, 2207, doi:10.1029/2001JB000896.

- Funicello, F., Moroni, M., Piromallo, C., Faccenna, C., Cendese, A. & Bui, H.A., 2006. Mapping mantle flow during retreating subduction: laboratory models analyzed by feature tracking, *J. geophys. Res.*, **111**, doi:10.1029/2005JB003792.
- Gledhill, K. & Gubbins, D., 1996. SKS splitting and the seismic anisotropy of the mantle beneath the Hikurangi subduction zone, New Zealand, *Phys. Earth planet. Inter.*, **95**, 227–236.
- Gripp, A.E. & Gordon, R.G., 2002. Young tracks of hot spots and current plate velocities, *Geophys. J. Int.*, **150**, 321–361.
- Gudmundsson, O. & Sambridge, M., 1998. A regionalized upper mantle (RUM) seismic model, *J. geophys. Res.*, **103**, 7121–7136.
- Hall, C., Fischer, K.M., Parmentier, E.M. & Blackman, D.K., 2000. The influence of plate motions on three-dimensional back arc mantle flow and shear wave splitting, *J. geophys. Res.*, **105**, 28 009–28 033.
- Harmon, N., Forsyth, D. W., Fischer, K.M. & Webb, S.C., 2004. Variations in shear-wave splitting in young Pacific seafloor, *Geophys. Res. Lett.*, **31**, doi:10.1029/2004GL020495.
- Hartog, R. & Schwartz, S., 2000. Subduction-induced strain in the upper mantle east of the Mendocino triple junction, California, *J. geophys. Res.*, **105**, 7909–7930.
- Helffrich, G., Wiens, D.A., Vera, E., Barrientos, S., Shore, P., Robertson, S. & Adaros, R., 2002. A teleseismic shear-wave splitting study to investigate mantle flow around South America and implications for plate-driving forces, *Geophys. J. Int.*, **149**, F1–F7.
- Heuret, A. & Lallemand, S., 2005. Plate motions, slab dynamics and back-arc deformation, *Phys. Earth planet. Inter.*, **149**, 31–51.
- Holtzmann, B.K., Kohlstedt, D.L., Zimmerman, M.E., Heidelbach, F., Hiraga, T. & Hustoft, J., 2003. Melt segregation and strain partitioning: implications for seismic anisotropy and mantle flow, *Science*, **301**, 1227–1230.
- Jech, J. & Pšenčík, I., 1989. First-order perturbation method for anisotropic media, *Geophys. J. Int.*, **99**, 369–376.
- Jung, H. & Karato, S.-i., 2001. Water-induced fabric transitions in olivine, *Science*, **293**, 1460–1463.
- Kaminski, É., 2002. The influence of water on the development of lattice preferred orientation in olivine aggregates, *Geophys. Res. Lett.*, **29**, doi:10.1029/2002GL014710.
- Kaminski, É. & Ribe, N.M., 2001. A kinematic model for recrystallization and texture development in olivine polycrystals, *Earth planet. Sci. Lett.*, **189**, 253–267.
- Kaminski, É. & Ribe, N.M., 2002. Timescales for the evolution of seismic anisotropy in mantle flow, *Geochem. Geophys. Geosyst.*, **3**, doi:10.1029/2001GC000222.
- Kaminski, É., Ribe, N.M. & Browaeys, J.T., 2004. D-Rex, a program for calculation of seismic anisotropy due to crystal lattice preferred orientation in the convective upper mantle, *Geophys. J. Int.*, **158**, 744–752.
- Karato, S.-i., 1992. On the Lehmann discontinuity, *Geophys. Res. Lett.*, **19**, 2255–2258.
- Karato, S.-i., 2003. Mapping water content in the upper mantle, in *Inside the Subduction Factory*, pp. 135–152, ed. Eiler, J.M., *Am. Geophys. Union. Geophys. Monogr. Ser.* 138.
- Katayama, I. & Karato, S., 2007. The effect of water on low temperature rheology of olivine, *J. geophys. Res.*, submitted.
- Katayama, I., Jung, H. & Karato, S.-i., 2004. New type of olivine fabric from deformation experiments at modest water content and low stress, *Geology*, **32**, 1045–1048.
- Katayama, I., Karato, S. & Brandon, M., 2005. Evidence of high water content in the deep upper mantle inferred from deformation microstructures, *Geology*, **33**, 613–616.
- Kelemen, P. B., Rilling, J.L., Parmentier, E.M., Mehl, L. & Hacker, B. R., 2003. Thermal structure due to solid-state flow in the mantle wedge beneath arcs, in *Inside the Subduction Factory*, pp. 223–276, ed. Eiler, J.M., *Am. Geophys. Union. Geophys. Monogr. Ser.* 138.
- Kellogg, L.H. & King, S.D., 1997. The effect of temperature dependent viscosity on the structure of new plumes in the mantle: results of a finite element model in a spherical, axisymmetric shell, *Earth planet. Sci. Lett.*, **148**, 12–26.
- Kennett, B.L.N. & Engdahl, E.R., 1991. Traveltimes for global earthquake location and phase identification, *Geophys. J. Int.*, **105**, 429–465.
- Kincaid, C. & Griffiths, R.W., 2004. Variability in flow and temperatures within mantle subduction zones, *Geochem. Geophys. Geosyst.*, **5**, doi:10.1029/2003GC000666.
- Kincaid, C. & Sacks, I.S., 1997. Thermal and dynamical evolution of the upper mantle in subduction zones, *J. geophys. Res.*, **102**, 12 295–12 315.
- King, S. D. & Hager, B.H., 1990. The relationship between plate velocity and trench viscosity in Newtonian and power-law subduction calculations, *Geophys. Res. Lett.*, **17**, 2409–2412.
- King, S.D., Raefsky, A. & Hager, B.H., 1990. ConMan: vectorizing a finite element code for incompressible two-dimensional convection in the Earth's mantle, *Phys. Earth planet. Inter.*, **59**, 195–207.
- King, S.K., 1991. The interaction of subducting slabs and the 670 km discontinuity, *Ph.D. thesis*, California Institute of Technology.
- Kneller, E.A., van Keken, P.E., Karato, S.-i. & Park, J., 2005. B-type olivine fabric in the mantle wedge: insights from high-resolution non-Newtonian subduction zone models, *Earth planet. Sci. Lett.*, **237**, 781–797.
- Kneller, E.A., Long, M.D., van Keken, P. E., Syracuse, E. & Abers, G., 2006. Olivine fabric transitions and shear-wave anisotropy in the Ryukyu subduction system, *Eos Trans. AGU*, **87**(52), Fall Meet. Suppl., Abstract U13B-02.
- Kneller, E.A., van Keken, P.E., Katayama, I. & Karato, S.-i., 2007. Stress, strain, and B-type olivine fabric in the fore-arc mantle: sensitivity tests using high-resolution steady-state subduction zone models, *J. geophys. Res.*, **112**, doi:10.1029/2006JBO04544.
- Kohlstedt, D.L., Evans, B. & Mackwell, S.J., 1995. Strength of the lithosphere: constraints imposed by laboratory experiments, *J. geophys. Res.*, **100**, 17 587–17 602.
- Kumazawa, M. & Anderson, O.L., 1968. Elastic moduli, pressure derivatives, and temperature derivatives of single-crystal olivine and single-crystal forsterite, *J. geophys. Res.*, **74**, 5961–5972.
- Lallemand, S., Heuret, A. & Boutelier, D., 2005. On the relationships between slab dip, back-arc stress, upper plate absolute motion, and crustal nature in subduction zones, *Geophys. Geochem. Geosyst.*, **6**, doi:10.1029/2005GC000917.
- Lassak, T.M., Fouch, M.J., Hall, C.E. & Kaminski, É., 2006. Seismic characterization of mantle flow in subduction systems: can we resolve a hydrated mantle wedge? *Earth planet. Sci. Lett.*, **243**, 632–649.
- Levin, V., Menke, W. & Park, J., 1999. Shear wave splitting in the Appalachians and the Urals: a case for multilayered anisotropy, *J. geophys. Res.*, **104**, 17 975–17 993.
- Levin, V., Droznin, D., Park, J. & Gordeev, E., 2004. Detailed mapping of seismic anisotropy with local shear waves in southeastern Kamchatka, *Geophys. J. Int.*, **158**, 1009–1023.
- Li, C., Van Der Hilst, R.D. & Toksöz, M.N., 2006. Constraining P-wave velocity variations in the upper mantle beneath Southeast Asia, *Phys. Earth planet. Inter.*, **154**, 180–195.
- Long, M.D. & Van Der Hilst, R.D., 2005. Upper mantle anisotropy beneath Japan from shear wave splitting, *Phys. Earth planet. Inter.*, **151**, 206–222.
- Long, M. D. & Van Der Hilst, R.D., 2006. Shear wave splitting from local events beneath the Ryukyu Arc: trench-parallel anisotropy in the mantle wedge, *Phys. Earth planet. Inter.*, **155**, 300–312.
- Long, M.D., de Hoop, M.V. & Van Der Hilst, R.D., 2007. Wave-equation shear wave splitting intensity tomography, *Geophys. J. Int.*, submitted.
- Malvern, L. E., 1969. *Introduction to the Mechanics of a Continuous Media*, Prentice-Hall, Englewood Cliffs, NJ.
- Margheriti, L., Nostro, C., Cocco, M. & Amato, A., 1996. Seismic anisotropy beneath the Northern Apennines (Italy) and its tectonic implications, *Geophys. Res. Lett.*, **23**, 2721–24.
- McKenzie, D., 1979. Finite deformation during fluid flow, *Geophys. J. R. astr. Soc.*, **58**, 689–715.
- Mensch, T. & Rasolofosaon, P., 1997. Elastic-wave velocities in anisotropic media of arbitrary symmetry – generalization of Thomsen's parameters ε , δ , and γ , *Geophys. J. Int.*, **128**, 43064.
- Mizukami, T., Wallis, S.R. & Yamamoto, J., 2004. Natural examples of

- olivine lattice preferred orientation patterns with a flow-normal a-axis maximum, *Nature*, **427**, 432–36.
- Nakajima, J. & Hasegawa, A., 2004. Shear-wave polarization anisotropy and subduction-induced flow in the mantle wedge of northern Japan, *Earth planet. Sci. Lett.*, **225**, 365–77.
- Nakajima, J., Shimizu, J., Hori, S. & Hasegawa, A., 2006. Shear-wave splitting beneath the southwestern Kurile arc and northeastern Japan arc: a new insight into mantle return flow, *Geophys. Res. Lett.*, **33**, doi:10.1029/2005GL025053.
- Nakamura, M., Yoshida, Y., Zhao, D., Katao, H. & Nishimura, S., 2003. Three-dimensional P- and S-wave velocity structures beneath the Ryukyu arc, *Tectonophysics*, **369**, 121–143.
- Park, J. & Levin, V., 2002. Seismic anisotropy: tracing plate dynamics in the mantle, *Science*, **296**, 485–89.
- Peyton, V., Levin, V., Park, J., Brandon, M., Lees, J., Gordeev, E. & Ozerov, A., 2001. Mantle flow at a slab edge: seismic anisotropy in the Kamchatka region, *Geophys. Res. Lett.*, **28**, 379–82.
- Pozgay, S. H., Wiens, D.A., Conder, J.A., Shiobara, H. & Sugioka, H., 2007. Mantle flow throughout the Mariana subduction system from shear wave splitting, *Geophys. J. Int.*, in press.
- Ribe, N. M., 1992. On the relationship between seismic anisotropy and finite strain, *J. geophys. Res.*, **97**, 8737–8748.
- Rupke, L.H., Phipps Morgan, J., Hort, M. & Connolly, J.A.D., 2004. Serpentine and the subduction zone water cycle, *Earth planet. Sci. Lett.*, **223**, 17–34.
- Russo, R.M. & Silver, P.G., 1994. Trench-parallel flow beneath the Nazca Plate from seismic anisotropy, *Science*, **263**, 1105–1111.
- Saltzer, R.L., Gaherty, J. & Jordan, T.H., 2000. How are vertical shear wave splitting measurements affected by variations in the orientation of azimuthal anisotropy with depth? *Geophys. J. Int.*, **141**, 374–390.
- Schulte-Pelkum, V. & Blackman, D.K., 2003. A synthesis of seismic P and S anisotropy, *Geophys. J. Int.*, **154**, 166–178.
- Silver, P.G. & Savage, M.K., 1994. The interpretation of shear-wave splitting parameters in the presence of two anisotropic layers, *Geophys. J. Int.*, **119**, 949–963.
- Skemer, P., Katayama, I. & Karato, S.-i., 2006. Deformation fabrics of the Cima di Gagnone peridotite massif, Central Alps, Switzerland: evidence of deformation at low temperatures in the presence of water, *Contrib. Mineral. Petr.*, **152**, 43–51.
- Smith, G.P., Wiens, D.A., Fischer, K.M., Dorman, L.M., Webb, S.C. & Hildebrand, J.A., 2001. A complex pattern of mantle flow in the Lau Backarc, *Science*, **292**, 713–716.
- Stacey, F. D., 1992. *Physics of the Earth*, Brookfield Press, Brisbane, Australia.
- Stern, R.J., 2002. Subduction zones, *Rev. Geophys.*, **40**, doi:10.1029/2001RG000108.
- Syracuse, E.M. & Abers, G.A., 2006. Global compilation of variations in slab depth beneath arc volcanoes and implications, *Geochem. Geophys. Geosyst.*, **7**, doi:10.10129/2005GC001045.
- Tackley, P.J., 1993. Effects of strongly temperature-dependent viscosity on time-dependent, 3-dimensional models of mantle convection, *Geophys. Res. Lett.*, **20**, 2187–2190.
- Thomsen, L., 1986. Weak elastic anisotropy, *Geophysics*, **51**, 1954–1966.
- Turcotte, D.L. & Schubert, G., 1982. *Geodynamics: Applications of Continuum Physics to Geological Problems*, John Wiley & Sons, New York.
- van Keken, P.E., 2003. The structure and dynamics of the mantle wedge, *Earth planet. Sci. Lett.*, **215**, 323–338.
- van Keken, P.E., Kiefer, B. & Peacock, S., 2000. High resolution models of subduction zones: implications for mantle dehydration reactions and the transport of water into the deep mantle, *Geochem. Geophys. Geosyst.*, **3**, doi:10.1029/2002GL015390.
- Wiens, D. A. & Smith, G. P., 2003. Seismological constraints on structure and flow patterns within the mantle wedge, in *Inside the Subduction Factory*, pp. 59–81, ed. Eiler, J.M., *Am. Geophys. Union. Geophys. Monogr. Ser.* 138.
- Wolfe, C. J. & Solomon, S. C., 1998. Shear-wave splitting and implications for mantle flow beneath the MELT region of the East Pacific Rise, *Science*, **280**, 1230–1232.
- Zhang, S. & Karato, S.-i., 1995. Lattice preferred orientation of olivine aggregates deformed in simple shear, *Nature*, **375**, 774–777.
- Zhong, S., Zuber, M.T., Moresi, L. & Gurnis, M., 2000. Role of temperature-dependent viscosity and surface plates in spherical shell models of mantle convection, *J. geophys. Res.*, **105**, 11 063–11 082.